Supplementary Information

Gold nanocrystals-loaded 2D supramolecular network for plasmon-enhanced nitrogen fixation

Gengxin Wang, Bingjin Li, Bao Li, and Lixin Wu**

State Key Laboratory of Supramolecular Structure and Materials, College of Chemistry, Jilin University, Changchun 130012, P. R. China.
**E-mail: wulx@jlu.edu.cn; libao@jlu.edu.cn*

Table of Contents

S1. Detailed materials

Cetyltrimethylammonium bromide (CTAB), sodium borohydride ($NaBH_4$), Chloroauric acid trihydrate ($HAuCl_4 \cdot 3H_2O$), silver nitrate ($AgNO_3$), ascorbic acid (AA), deuterium reagents (D_2O, $CDCl_3$, DMSO-d_6) were purchased from Sigma-Aldrich. The β-CD used in this study was purchased from Aladdin and recrystallized three times before use. p-toluene sulfonyl chloride (Ts-Cl), sodium azide (NaN_3), p-phenyldiacetylene, sodium ascorbate, copper sulfate pentahydrate ($CuSO_4 \cdot 5H_2O$), adamantanecarboxylic acid, dimethylethanolamine, methanesulfonic acid and iodomethane were all purchased from Aladdin. $H_4SiW_{12}O_{40}$ (SiW_{12}) was purchased from Aladdin. $K_4PW_{11}VO_{40}$ ($PW_{11}V$)[1] and $H_4PMo_{11}VO_{40}$ ($PMo_{11}V$)[2] were prepared according to the literature. The organic solvents used in the experiment were purchased from Beijing Chemical Reagent Company. The water used in the experiment was doubly distilled water.

S2. Measurements

^{1}H NMR spectra were collected from Bruker AVANCE 500 MHz and Zhongke-Niujin AS 400 MHz spectrometer. MALDI-TOF mass spectrometry was collected in an autoflex MALDI-TOF mass spectrometer (Bruker) equipped with a nitrogen laser (337 nm, 3 ns pulse). Fourier transform infrared (FT-IR) spectra was measured on the Bruker Vertex 80V FT-IR spectrometer. The ultraviolet-visible (UV-Vis) spectrum was measured on the Lambda 365 spectrometer. The UV-Vis diffuse reflection spectrum (UV-Vis DRS) was measured on the UV-Vis-near infrared absorption spectrometer (Lambda 1050+). Transmission electron microscopy (TEM) and element mapping were measured on the JEM 2010 under an accelerating voltage of 200 kV. Atom force microscopy (TEM) images were measured on the Icon-XR instrument. X-ray photoelectron spectra (XPS) and valence band spectra was measured on the ESCALAB-250 spectrometer using a monochromatic X-ray source (Al Kα line, 1486.6eV), and the peak was corrected using the C 1s binding energy position of 284.6eV. Powder X-ray diffraction (PXRD) data are collected on a Rigaku X-ray diffractometer using Cu Kα radiation at a wavelength of 1.542 Å. The analysis of inorganic elements was measured on an inductively coupled plasma spectrometer (ICP, OPTIMA 3300DV, Perkin Elmer, Germany). Organic element analysis is performed on the element analyzer Vario micro cube (Elementar, Germany). Dynamic Light scattering (DLS) and ZETA potential measurements were made on the Zetasizer NanoZS instrument (Malvern Instruments). Isothermal titration calorimeter (ITC) data were obtained using a MicroCal VP isothermal titration calorimeter (Malvern, UK). The visible light photocatalysis experiment uses a white LED lamp as the light source with a power of 70 W. Near infrared photothermal conversion experiment uses 808 nm laser light source with adjustable output power (Xi'an Hongxiang Laser Technology Co., Ltd.). N_2 absorption experiment was carried out on a ASAP2460 instrument (Micromeritics) at 77 K.

Photoelectrochemical measurement

The electrochemical measurements were conducted in a three electrode system on an electrochemical workstation (CHI 760EShanghai Chenhua). The working electrode was prepared as follows: the catalyst (0.002 mmol) was dispersed in a 200 μL ethanolic solution of Nafion (5.0 vol%). The dispersion was then dip-coated on a 1 cm × 3 cm ITO glass electrode and allowed to dry

in a vacuum overnight at room temperature. A Pt plate and standard Ag/AgCl electrode were employed as the counter and reference electrodes, respectively. The photoelectrochemical test was carried out in an Na_2SO_4 aqueous solution (40 mL, 0.1 M) electrolyte.

^{15}N isotopic labeling experiment

The isotopic labeling experiment used $^{15}N_2$ as feeding gas with the ^{15}N enrichment of 98% (Wuhan Isotope Technology Co., Ltd.). After photocatalytic $^{15}N_2$ fixation was conducted over AuNR@iHG-PMoV for 12 h, 1 mL of the mixture was withdrawn and the catalyst was separated by centrifugation (12000 r/min, 3 min). The pH of the solution was adjusted with 0.2 M HCl to 2–3. Then 0.2 mL of the above solution were added into 0.5 mL of the DMSO-d_6. The produced $^{15}NH_4^+$ and $^{14}NH_4^+$ were identifed using ^{1}H NMR spectroscopy (AVANCE 500 MHz, Bruker).

Measurement of NIR photothermal property

1.0 mL of AuNR@iHG-POM (0.2 mM) aqueous solution was placed in a quartz bottle. The solution was irradiated by a NIR laser (808 nm, 1.0 W cm^{-2}) under dark environment, and the temperature of the solution gradually increased until it remained constant. The laser was then turned off. The temperature change during this period was recorded with a thermal imaging camera every 30 s. Under the same condition, the heating and cooling processes of 1.0 mL of blank water were recorded as the control to calculate the efficiency of photothermal conversion.

Measurement of visible light-driven catalysis

AuNP@iHG-PWV (20 mg, 2.0 μmol) was dispersed in 10 mL of H_2SO_4 solution (0.5 mM) and sealed in a 25 mL quartz flask. N_2 (100 mL/min) was continuously pumped into the flask for 30 min in dark to expel air from the system, and then a white LED light (420−700 nm, 70 W) was turned on to start the reaction. 1.0 mL of reaction solution was taken out every 10 min for measurement until the reaction time reached 1 h. The catalyst was separated by centrifugation, and then 4.0 mL of H_2SO_4 solution (0.5 mM) was added. The amount of the generated NH_3 in the system was then detected by indophenol blue method. As a control experiment, the reaction without light radiation was performed in dark.

Measurement of NIR light-driven photothermal catalysis

2.0 μmol of AuNR@iHG-POM (17.5 mg for AuNR@iHG-PWV, 15.0 mg for AuNR@iHG-PMoV, and 17.5 mg for AuNR@iHG-SiW) was dispersed in 10 mL of water and then sealed in a 25 mL of quartz flask. In the dark condition, N_2 (100 mL/min) was continuously pumped into the flask for 30 min, so that the system was completely under the atmosphere of N_2. The NIR laser (808 nm, 1.0 W cm^{-2}) radiation was performed for photothermal catalytic reaction. During the process, 1.0 mL of reaction solution was taken out every 10 min until the reaction time reached 1.0 h. The catalyst was separated by centrifugation and 4.0 mL of H_2SO_4 solution (0.5 mM) was added. The concentration of produced NH_3 was then detected by indophenol blue method. As a control experiment, the reaction was carried out at room temperature and external heating condition under dark environment.

S3. Materials preparation.

Preparation of bridging cyclodextrin (B-CD)

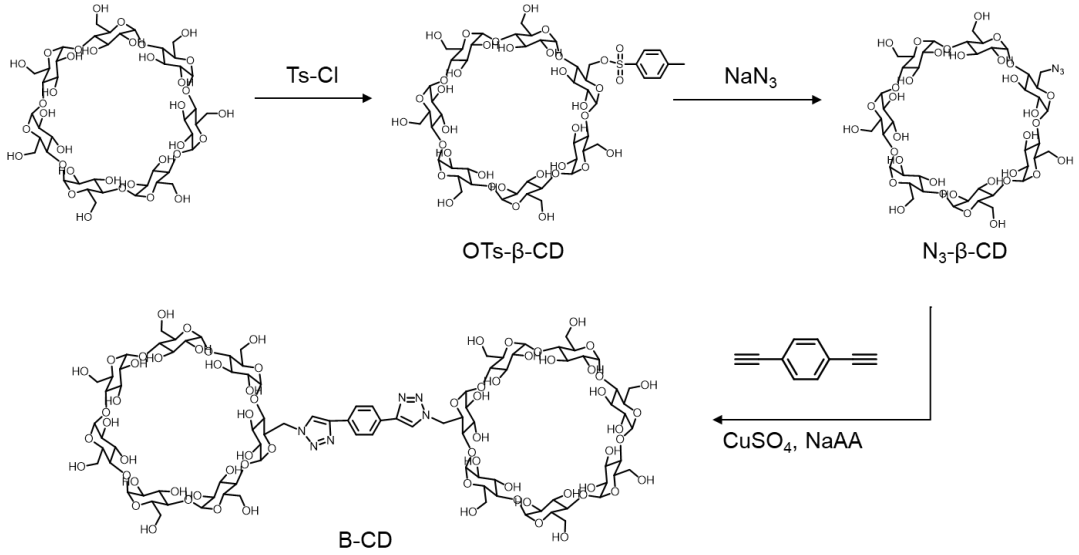

Scheme S1. Synthetic route of B-CD.

Synthesis of mono-6-N_3-β-CD (N_3-β-CD). Mono-6-OTs-β-CD (OTs-β-CD) was prepared according to the literature.[3] OTs-β-CD (1.5g) and NaN_3 (0.286 g) were dissolved in 20 mL dimethylformamide organic solvent. Then the solution was heated to 80°C and stirred overnight. After the reaction, the solution was cooled to room temperature, and then the mixed solvent of 10 mL water and 75 mL acetone was added to the solution. White precipitates appeared later. After filtration and washing with acetone, white solid product (1.2g) was obtained after drying with a yield of about 90%. ^{1}H NMR (500 MHz, DMSO-d_6) δ 5.74 (d, 14 H), 4.83 (d, 7 H), 4.62–4.43 (m, 6 H), 3.77 (s, 2 H), 3.72–3.47 (m, 26 H), 3.30 (d, 14 H). MALDI-TOF MS (m/z): 1183.2 $[M + Na]^+$, 1199.1 $[M + K]^+$.

Synthesis of B-CD. N_3-β-CD (500 mg), p-phenyldiacetylene (27.1 mg) and $CuSO_4 \cdot 5H_2O$ (215.5 mg) were dispersed in 30 mL of dimethylformamide solvent. Sodium ascorbate (341.4 mg) was dissolved in 10 mL dimethylformamide-water solution (DMF:H_2O = 4:1), and then the fresh sodium ascorbate solution was added drop by drop to the above dispersed solution while stirring. During this process a distinct color changed from green to orange. Then the solution was heated in a water bath at 30°C and stirred for 20 h. After that, the solution was cooled to room temperature, and then the solvent was removed under a reduced pressure to get the crude product. The product was purified by column chromatography with acetonitrile/water = 7/3. The pure product was white solid (131.8 mg) with a yield of about 25%. ^{1}H NMR (400 MHz, D_2O) δ 8.38 (s, 2 H), 7.90 (s, 4 H), 5.15 (s, 2 H), 5.05 (d, 9 H), 4.94 (dd, 4 H), 4.89 (d, 2 H), 4.64–4.56 (m, 9 H), 4.17 (t, 2 H), 4.03 (s, 2 H), 4.01–3.93 (m, 2 H), 3.96–3.75 (m, 32 H), 3.70–3.39 (m, 70 H), 3.31 (d, 2 H), 3.02 (d, 2 H), 2.79 (d, 2 H). MALDI-TOF MS (m/z): 2468.9 $[M + Na]^+$, 2485.0 $[M + K]^+$. Theoretical value of element analysis ($C_{94}H_{144}N_6O_{68}(H_2O)_8$): C: 43.59%, H: 6.23%, N: 3.24%, found: C: 44.02 %, H: 6.32%, N: 3.28%.

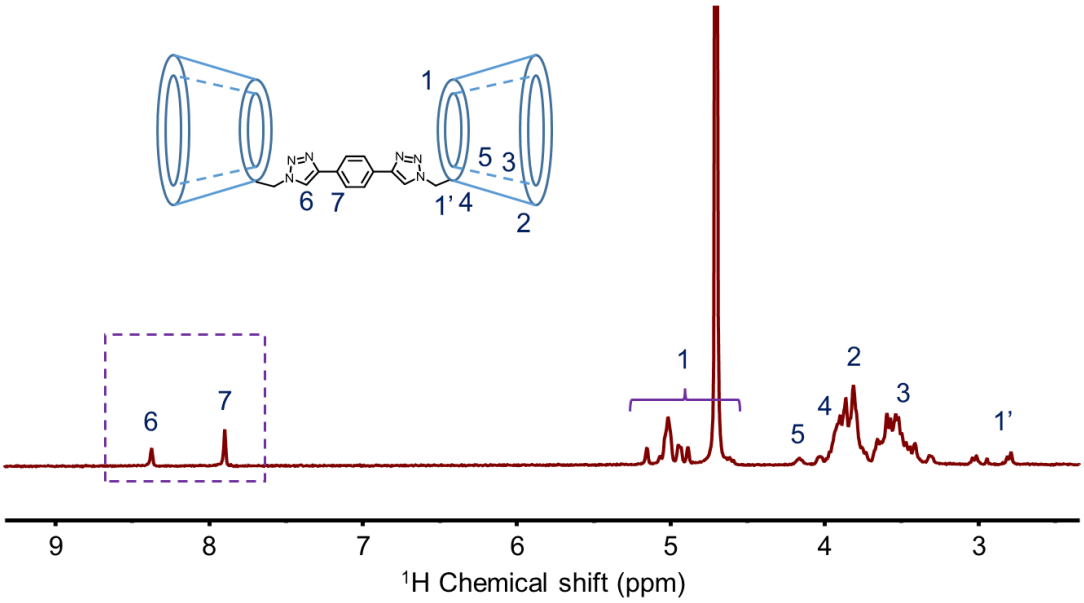

Fig. S1. ^{1}H NMR spectrum of B-CD (D_2O, 25°C).

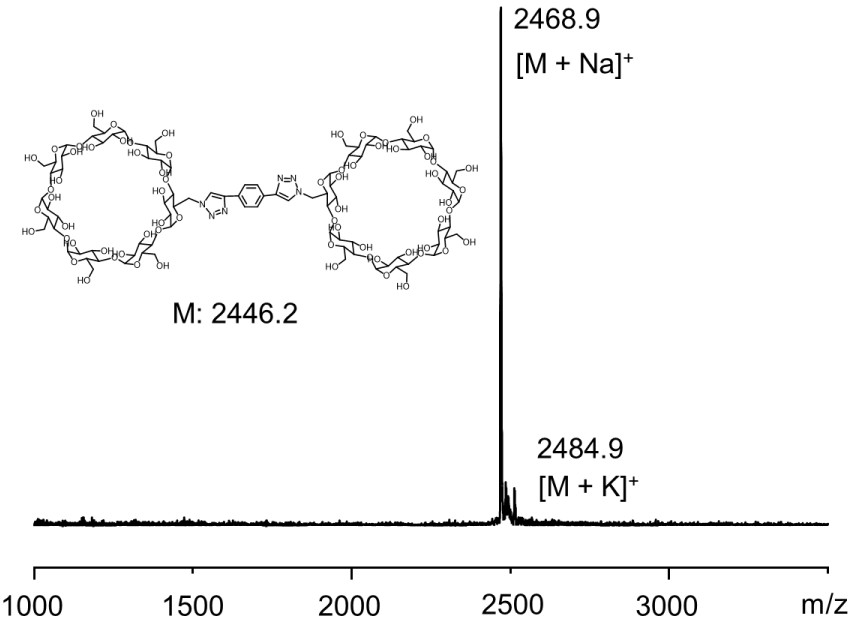

Fig. S2. MALDI-TOF mass spectrum of B-CD (CHCA as matrix).

Preparation of cation adamantane surfactant (C-AD)

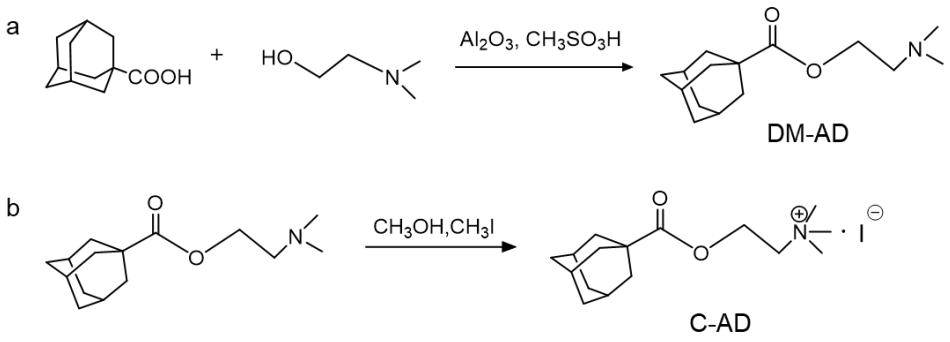

Scheme S2. Synthetic route of C-AD.

Synthesis of 2-(dimethylamino)ethyl-adamantane-1-carboxylate (DM-AD).

Adamantanecarboxylic acid (1.0 g), dimethylethanolamine (0.5 g, 0.57 mL), aluminum oxide (1.7 g) and methanesulfonic acid (5.4 mL) were added to a 50 ml round-bottomed flask. Then the mixture was stirred and heated to 90°C for 6 h. When the solution was cooled down to room temperature, the saturated sodium carbonate solution was slowly added to it until no bubbles emerge. Then it was extracted by ethyl acetate and the organic phase was separated and dried by anhydrous sodium sulfate. After filtration, the organic solvent was removed under a reduced pressure to get the yellow oily product (1.1 g) with a yield of about 80%. ^{1}H NMR (400 MHz, $CDCl_3$) δ 4.19 (td, 2 H), 2.60 (dd, 2 H), 2.32 (d, 6 H), 2.07–2.01 (m, 3 H), 1.92 (d, 6 H), 1.74 (q, 6 H).

Synthesis of C-AD. DM-AD (1.0 g) was dissolved in 4 mL anhydrous methanol and placed in a 50 mL round-bottomed flask. The iodomethane (0.75 mL) was slowly added drop by drop. The mixed solution was heated to 70°C and stirred for 4 h. After the reaction, the solution was cooled to room temperature, and the organic solvent was removed under a reduced pressure to obtain crude products. A small amount of ice ethanol solution was added to wash the solid to get the pure product (1.4 g) with a yield of about 90%. ^{1}H NMR (400 MHz, $CDCl_3$) δ 4.59 (t, 2 H), 4.19–4.13 (m, 2 H), 3.61 (s, 9 H), 2.06 (d, 3 H), 1.91 (d, 6 H), 1.75 (q, 6 H). MALDI-TOF MS (m/z): 266.3 $[M]^+$. Theoretical values of elemental analysis ($C_{16}H_{27}INO_2$): C: 48.99%, H: 6.94%, N: 3.57%, found: C: 48.82 %, H: 6.87%, N: 3.40%.

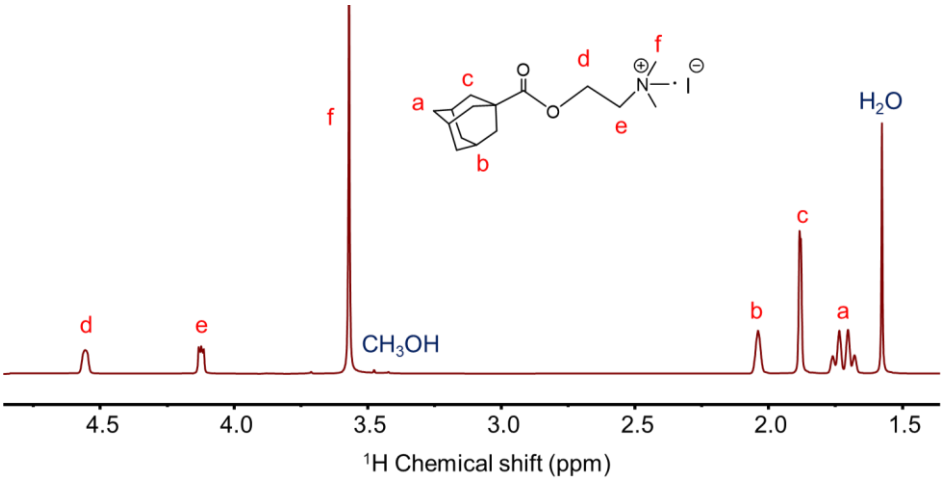

Fig. S3. ^{1}H NMR spectrum of C-AD ($CDCl_3$, 25°C).

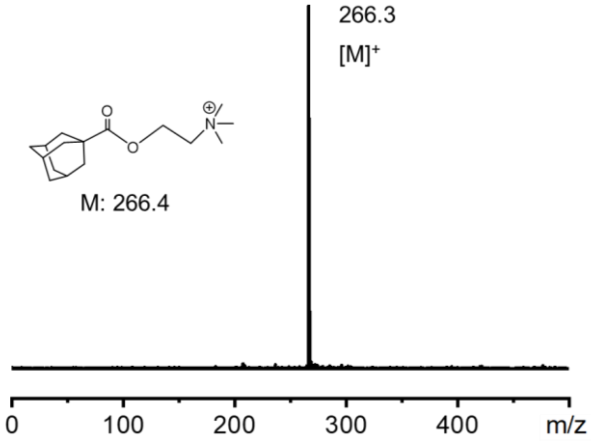

Fig. S4. MALDI-TOF mass spectrum of C-AD (DCTB as matrix).

Preparation of iHG-POMs.

Preparation of host-guest complexes. C-AD (6.3 mg, 1.6 μmol) was dissolved in 5 mL water and to the aqueous solution was added B-CD (19.8 mg, 0.8 μmol) dissolving in 5 mL of water with stirring. The resulting mixed solution was sonicated at room temperature for 30 min and left to stand overnight, obtaining the host-guest complex solution (0.8 mM).

Preparation of iHG-POMs. The POMs including $K_4PW_{11}VO_{40}$ ($PW_{11}V$), $H_4PMo_{11}VO_{40}$ ($PMo_{11}V$) and $H_4SiW_{12}O_{40}$ (SiW_{12}) were used to construct the ionic supramolecular frameworks with the prepared host-guest complexes through electrostatic interaction. $PW_{11}V$ and $PMo_{11}V$ were synthesized according to the literature. Firstly, 5 mL of above host-guest complex in aqueous solution was placed in a 50 mL conical flask. Then 0.4 μmol of POMs ($PW_{11}V$, $PMo_{11}V$ and SiW_{12}) in water (5 mL) was added dropwise with stirring. The mixture solution became significantly cloudy and was placed in a refrigerator (5°C) for 24 h for further assembling into supramolecular framework (iHG-PWV, iHG-PMoV and iHG-SiW) at the concentration of about 0.2 mM.

Preparation of AuNP@iHG-POM.

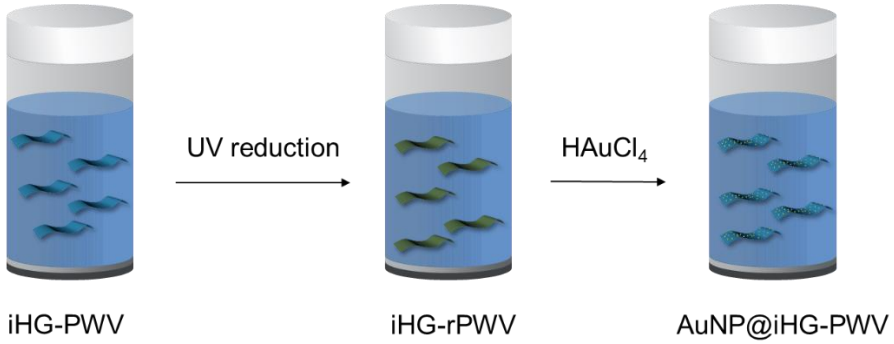

Scheme S3. Schematic of the preparation of AuNP@iHG-PWV.

By taking iHG-PWV as an example, the AuNP loaded composite, named as AuNP@iHG-PWV, was prepared with detailed steps as follows. 1.0 mL of iHG-PWV aqueous solution was placed in a quartz bottle and then irradiated by a LED UV curing lamp (365 nm, 10 W) for 10 min with stirring under the dark environment. The color of the solution changed significantly due to the reduction of POMs,[4] obtaining reduced iHG-rPWV. To the solution, 1.0 mL of fresh $HAuCl_4{\cdot}3H_2O$ aqueous solution (0.2 mM) was added while stirring (300 r/min), and the mixture was continuously stirred for another 1.0 h, allowing the in-situ production of AuNP on iHG-PWV assembly via a reduction reaction with the reduced $PW_{11}V$. The mixed solution was centrifuged and washed with water twice, giving the composite catalyst AuNP@iHG-PWV.

Preparation of AuNR@iHG-POM.

Thiol-substituted cation modified AuNRs (M-AuNRs) were prepared via a substitution procedure to the previously prepared cetyltrimethyl ammonium bromide protected gold nanorods (CTAB-AuNRs), which were prepared following published procedures.[5] Then, the positive charged M-AuNRs were adsorbed on the iHG-POM through the electrostatic interaction, forming AuNR-loaded iHG-POM composite catalyst, AuNR@iHG-POM. The detailed operation was as follows. 800 μL of M-AuNR aqueous solution (Au: 135 ppm) was added dropwise to 2.0 mL of the above

prepared iHG-POM (iHG-PWV, iHG-PMoV and iHG-SiW) aqueous solution (0.2 mM) while stirring (300 r/min). Then the mixed solution was stirred continuously for 1 h. After centrifugation and washing with water, the product was obtained.

S4. Host-guest and electrostatic interaction in iHG-POM.

The host-guest interaction is demonstrated by nuclear magnetic resonance (NMR) spectroscopy and isothermal titration calorimetry (ITC) test. Compared with the ^{1}H NMR spectrum of C-AD, the chemical shift of peaks (H_a, H_b and H_c) belonging to the adamantane unit in the host-guest complex moves to the lower field, indicating that the chemical environment around the C-AD changes. The 2D-nuclear Overhauser effect spectroscopic (2D NOESY) analysis between $H_{a–c}$ of C-AD and $H_{2–5}$ of B-CD further figures out the inclusion of adamantane into the cavity of B-CD. In addition, there is no correlation signal appearing between $H_{6–7}$ and $H_{2–5}$ of B-CD, which also proves that no self-inclusion occurs after the guest is added. Upon mixing with host B-CD, $H_{a–c}$ of C-AD shift downfield in the titration spectra. Based on the H_b shifting belonging adamantane peak, the inclusion ratio of C-AD to B-CD in forming host-guest complex is calculated to be 2:1 via a non-linear fitting method.[6] The measured ITC curves show that the binding constant of B-CD and C-AD is 4.28×10^4 M^{-1}, indicating a strong inclusion interaction. The calculated binding ratio from fitting is 2:1, which is consistent with the results of ^{1}H NMR titration plot.

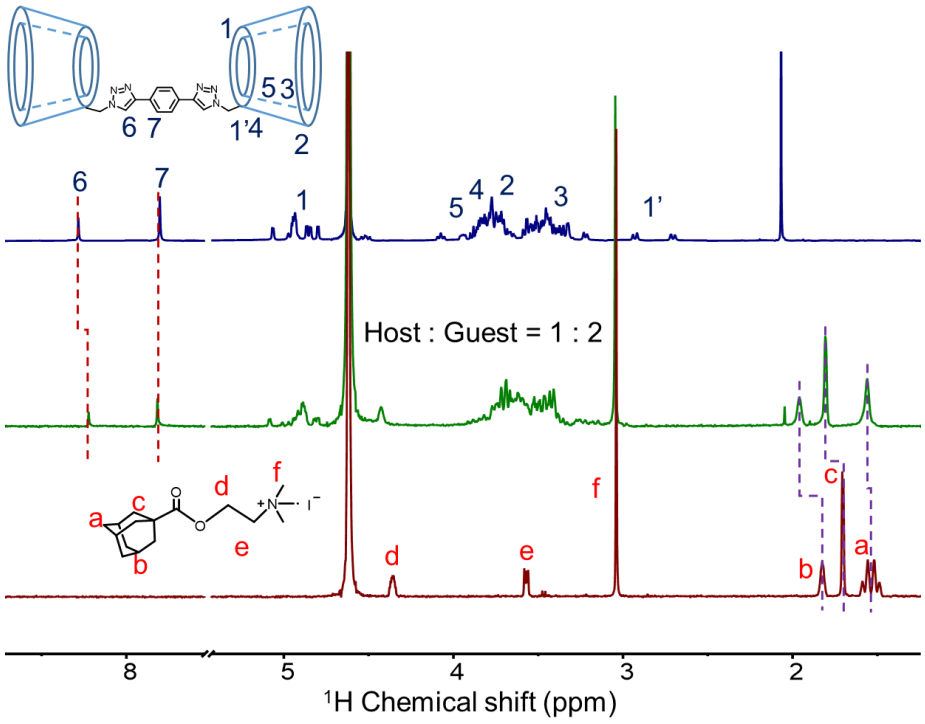

Fig. S5. Partial ^{1}H NMR spectra (D_2O, 500 MHz, 25°C) of B-CD (blue line), the host-guest complex (host: guest= 1:2) (green line) and C-AD (red line).

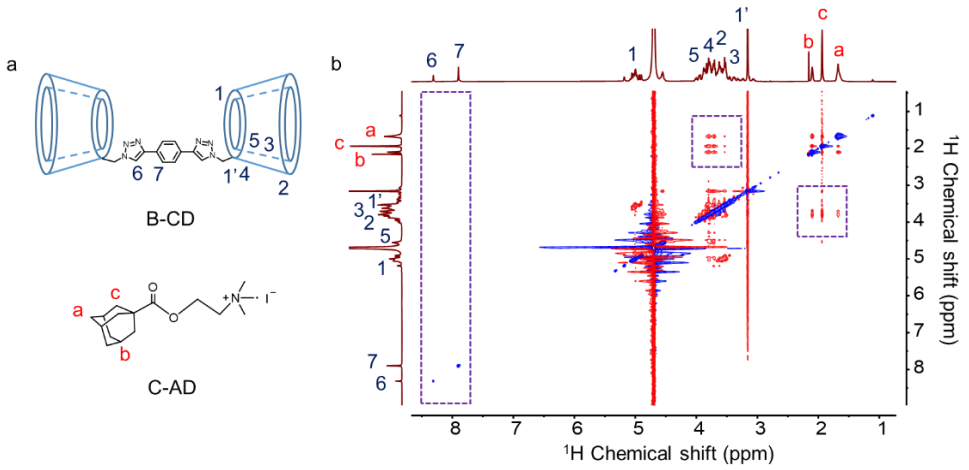

Fig. S6. (a) Molecular structure of B-CD and C-AD. (b) Partial 2D NOESY spectrum (D_2O, 500 MHz, 25°C) of host-guest complex between B-CD and C-AD (1:2).

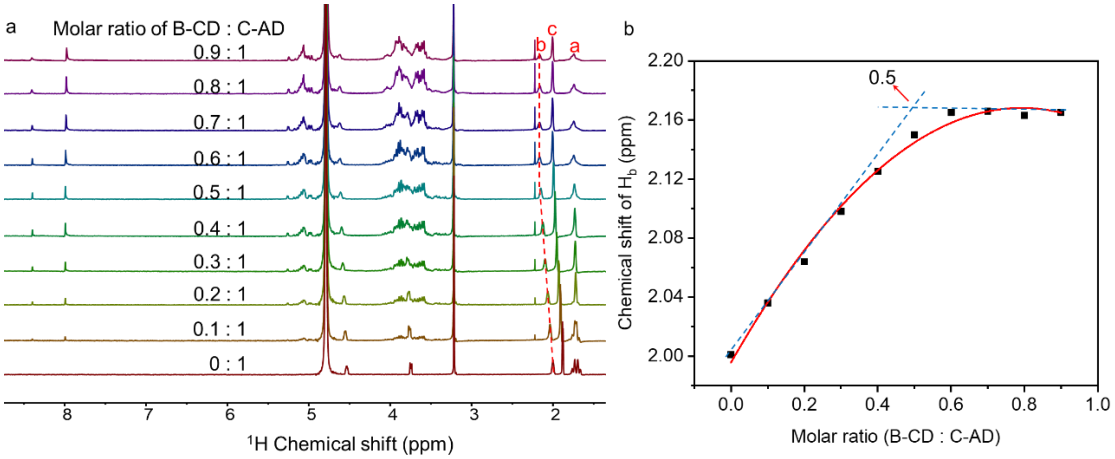

Fig. S7. ^{1}H NMR spectra of host-guest complexes with different molar ratios of B-CD:C-AD and (b) the corresponding plot of the chemical shift of H_b versus the above molar ratio changes.

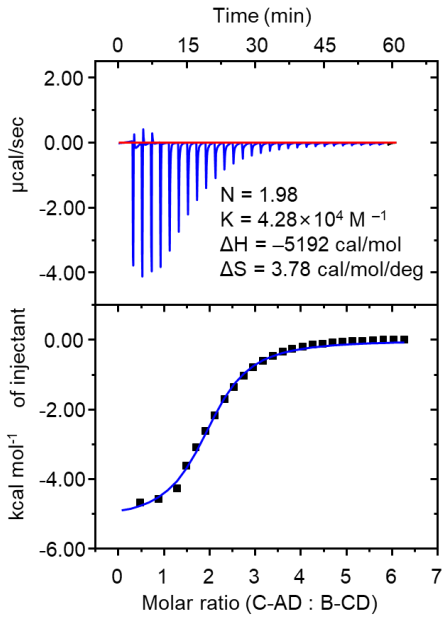

Fig. S8. ITC curve and fitting of C-AD (8 mM) titrating B-CD (0.2 mM) in water.

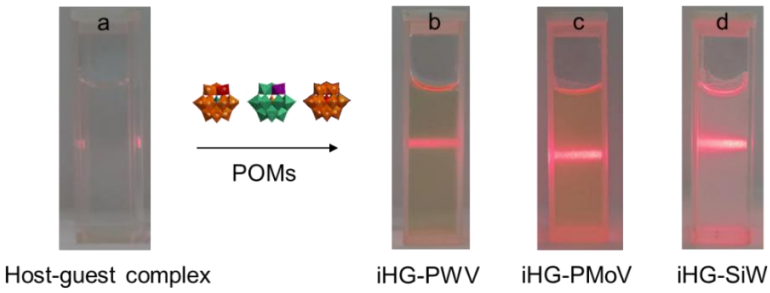

Fig. S9. Digital photographs of (a) host-guest complex of B-CD and C-AD, (b) iHG-PWV, (c) iHG-PMoV and (d) iHG-SiW aqueous solution.

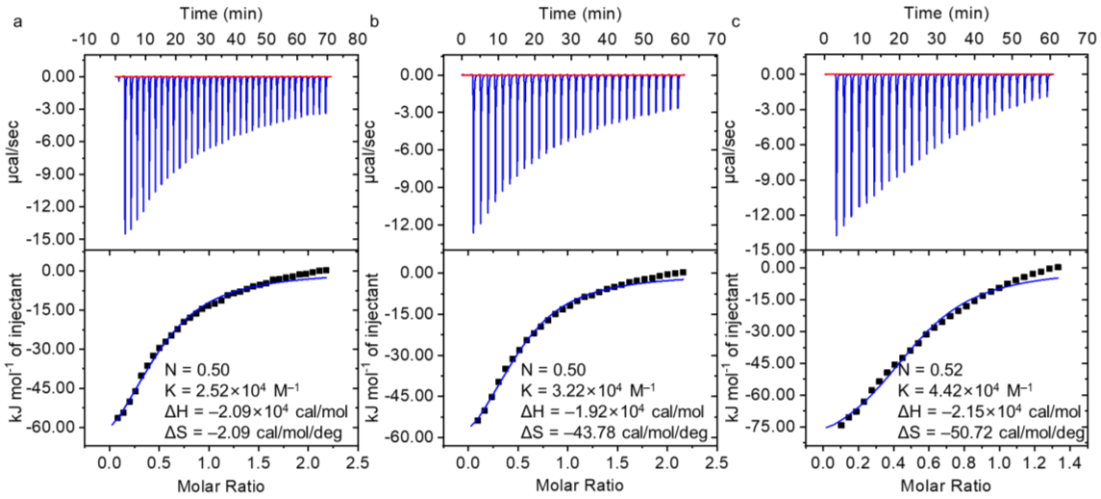

Fig. S10. ITC curves and fittings of (a) $PW_{11}V$, (b) $PMo_{11}V$ and (c) SiW_{12} (2 mM) titrating host-guest complex (0.15 mM) of B-CD and C-AD in water.

S5. Structure and morphologic characterization of the iHG-POM.

Table S1. Elemental analysis of iHG-PWV.

$C_{94}H_{144}N_6O_{68})_2(C_{16}H_{27}NO_2)_4PW_{11}VO_{40}$	N	C	H	P	W	V
Calculated (%)	2.58	34.79	4.59	0.36	23.25	0.58
Found (%)	2.59	34.15	4.62	0.45	23.98	0.50
Error (%)	0.01	0.64	0.03	0.09	0.73	0.08

Table S2. Elemental analysis of iHG-PMoV.

$C_{94}H_{144}N_6O_{68})_2(C_{16}H_{27}NO_2)_4PW_{11}VO_{40}$	N	C	H	P	Mo	V
Calculated (%)	2.90	39.15	5.16	0.40	13.65	0.66
Found (%)	2.85	39.37	5.32	0.42	13.74	0.61
Error (%)	0.05	0.22	0.16	0.02	0.09	0.05

Table S3. Elemental analysis of iHG-SiW.

$C_{94}H_{144}N_6O_{68})_2(C_{16}H_{27}NO_2)_4SiW_{12}O_{40}$	N	C	H	Si	W
Calculated (%)	2.54	34.28	4.52	0.32	24.99
Found (%)	2.62	35.90	4.57	0.38	24.52
Error (%)	0.08	1.62	0.05	0.06	0.47

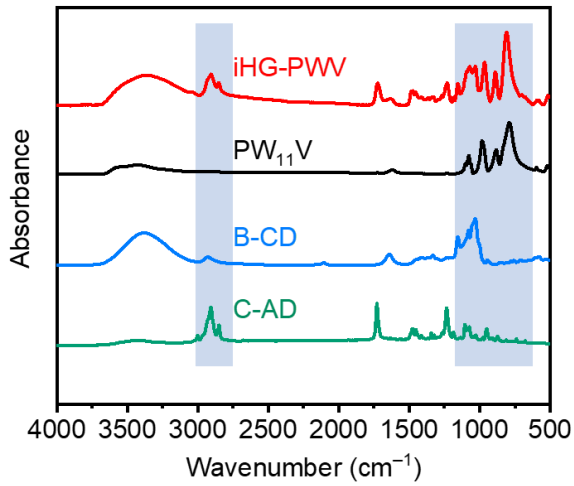

Fig. S11. FT-IR spectra of iHG-PWV, $PW_{11}V$, B-CD and C-AD.

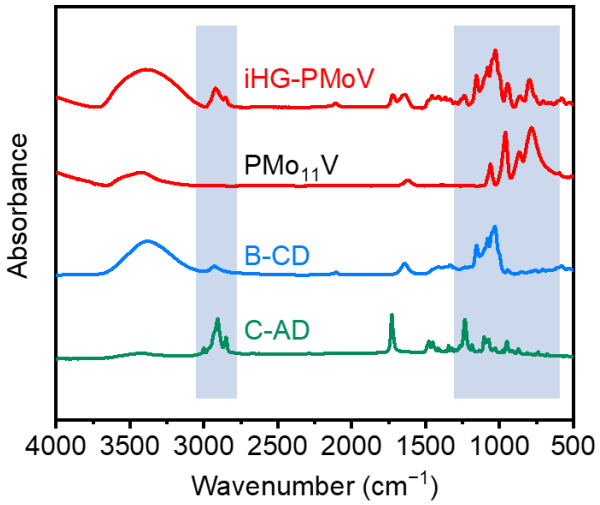

Fig. S12. FT-IR spectra of iHG-PMoV, $PMo_{11}V$, B-CD and C-AD.

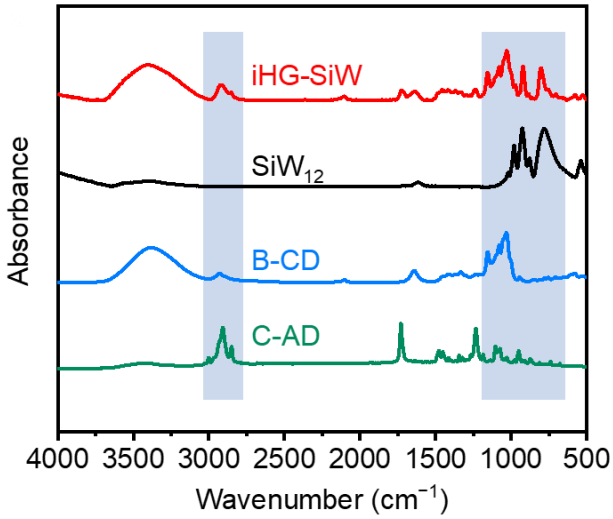

Fig. S13. FT-IR spectra of iHG-SiW, SiW_{12}, B-CD and C-AD.

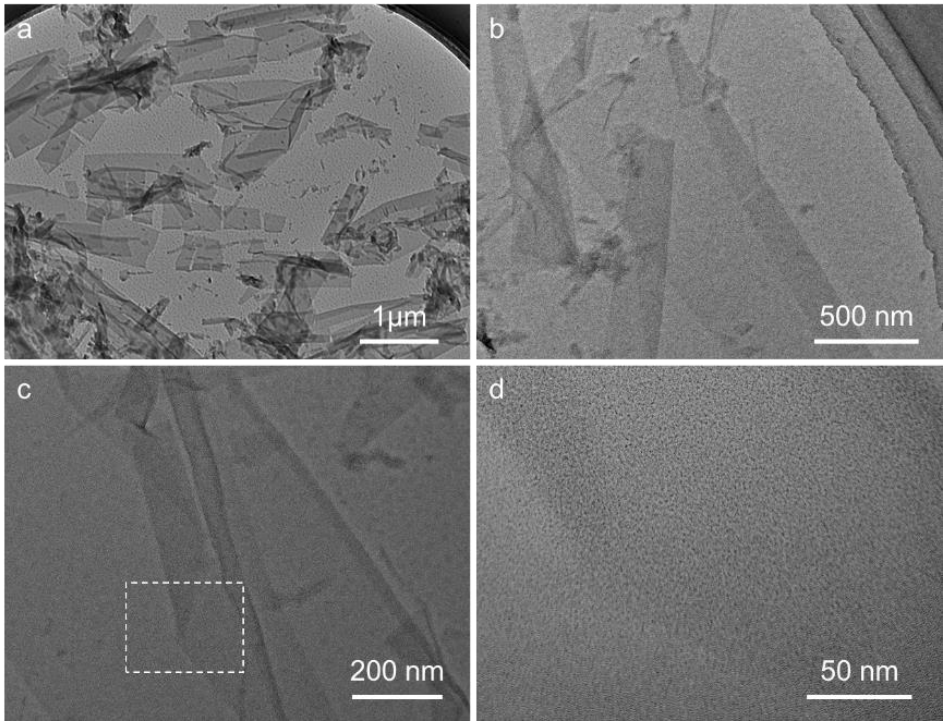

Fig. S14. TEM images of iHG-PMoV at (a–c) low and (d) high magnification.

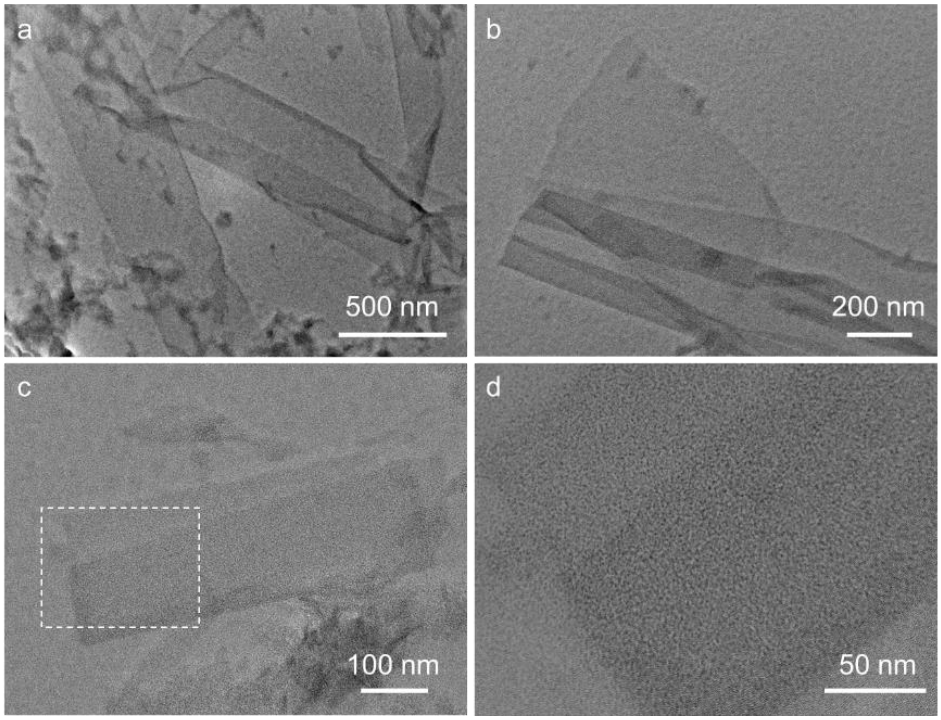

Fig. S15. TEM images of iHG-SiW at (a–c) low and (d) high magnification.

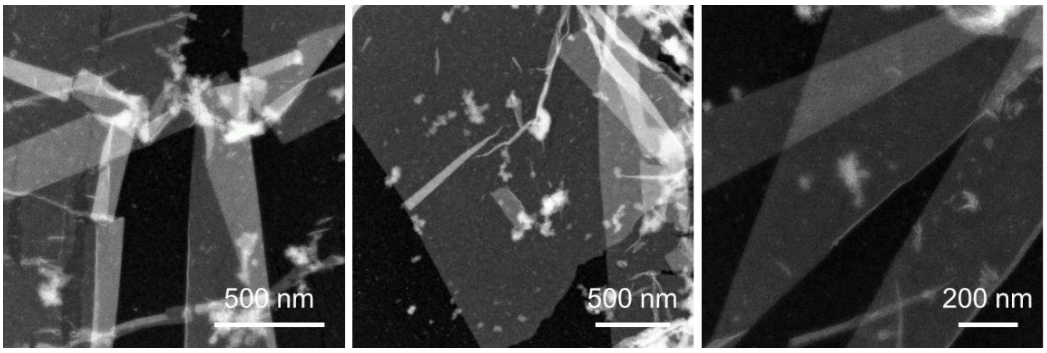

Fig. S16. HAADF-STEM images of iHG-PMoV.

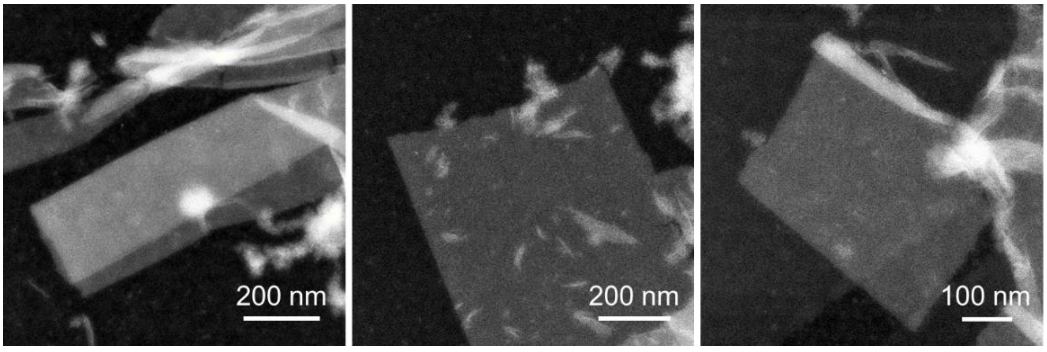

Fig. S17. HAADF-STEM images of iHG-SiW.

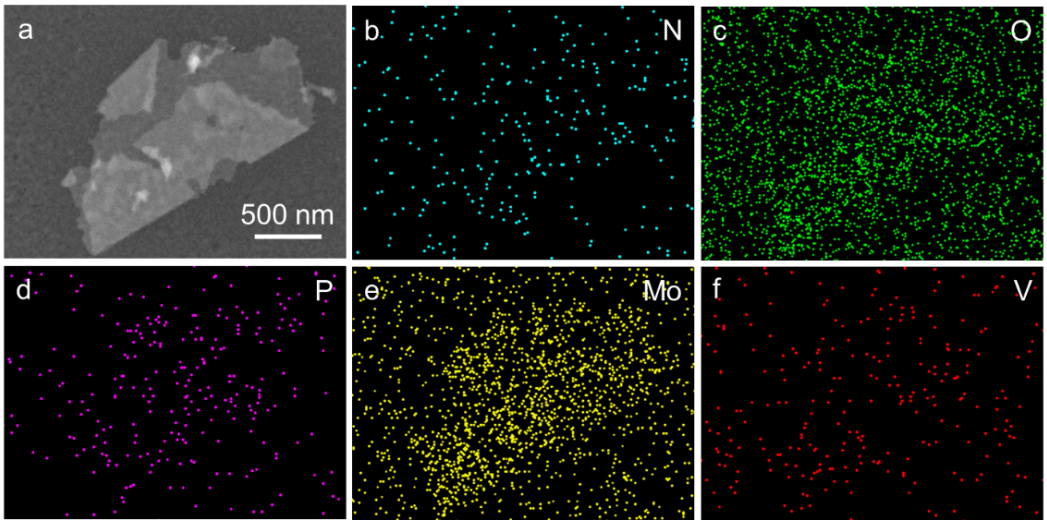

Fig. S18. (a) HAADF-STEM image of iHG-PMoV and (b–f) the corresponding elemental maps.

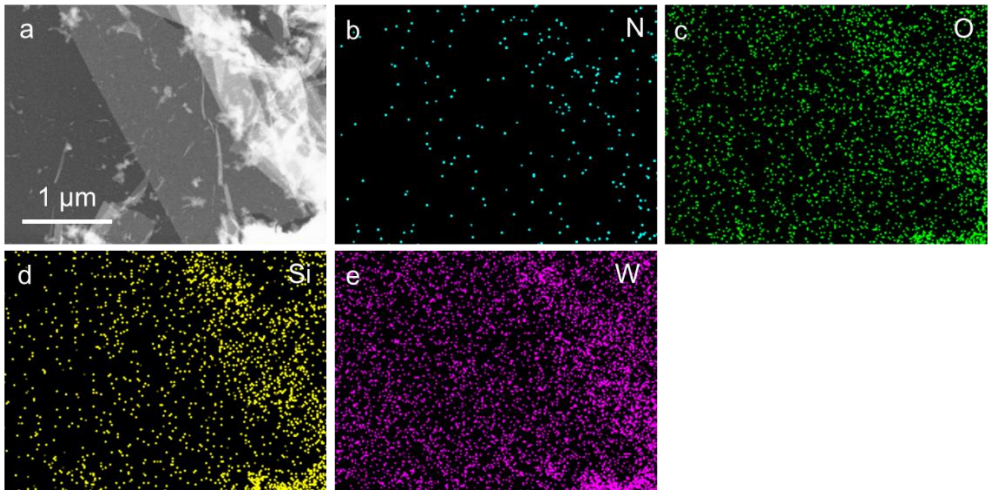

Fig. S19. (a) HAADF-STEM image of iHG-SiW and (b–e) the corresponding elemental maps.

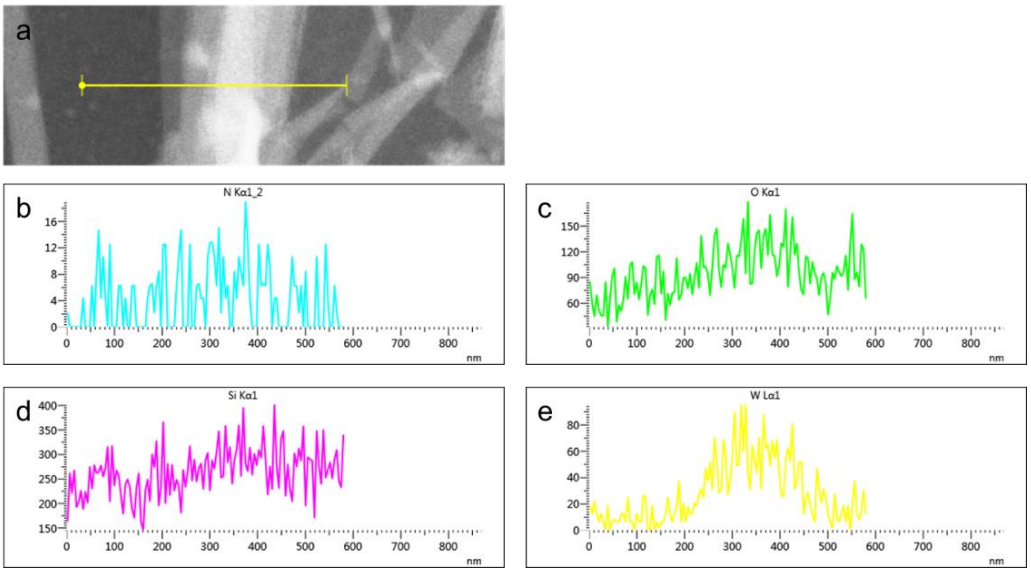

Fig. S20. (a) HAADF-STEM image of iHG-SiW and (b–e) the corresponding line-scan EDX analysis.

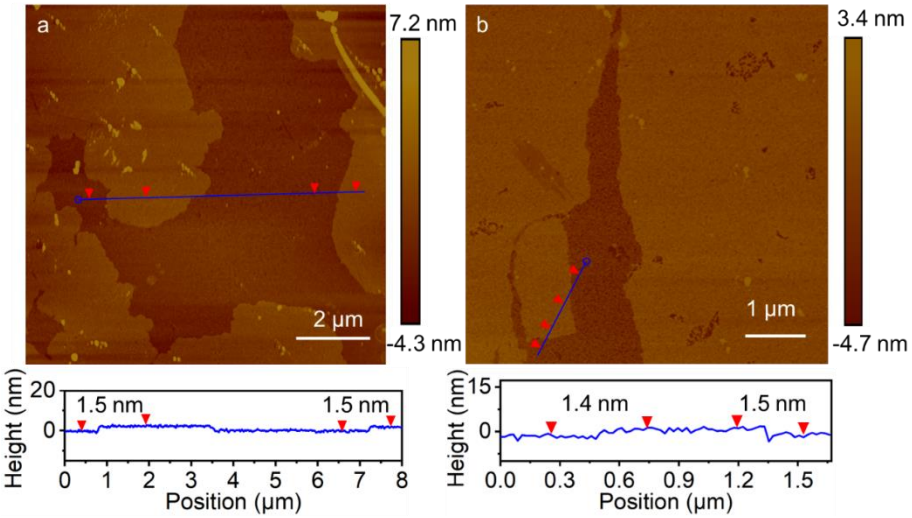

Fig. S21. AFM image and height profile analysis of (a) iHG-PMoV and (b) iHG-SiW.

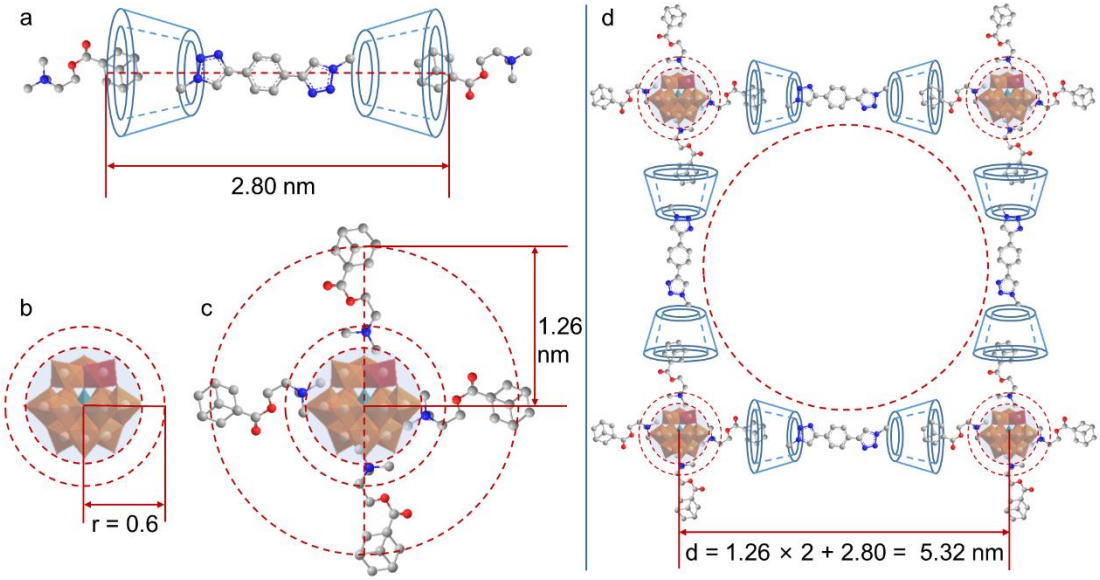

Fig. S22. Diagram of structure model of (a) host-guest complexes, (b) $PW_{11}VO_{40}$ cluster, (c) electrostatic bonding complexes of POM with C-AD, and (d) iHG-PWV.

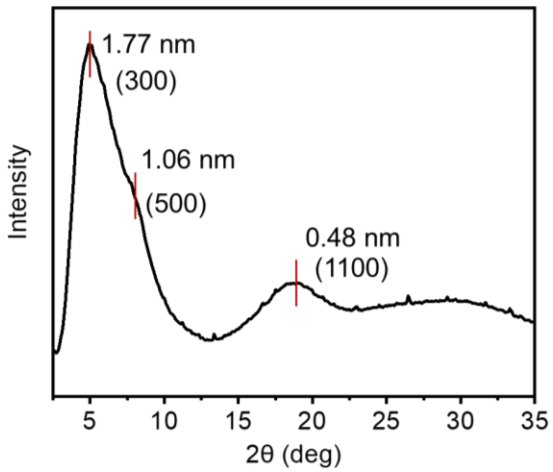

Fig.S23. PXRD pattern of iHG-PWV.

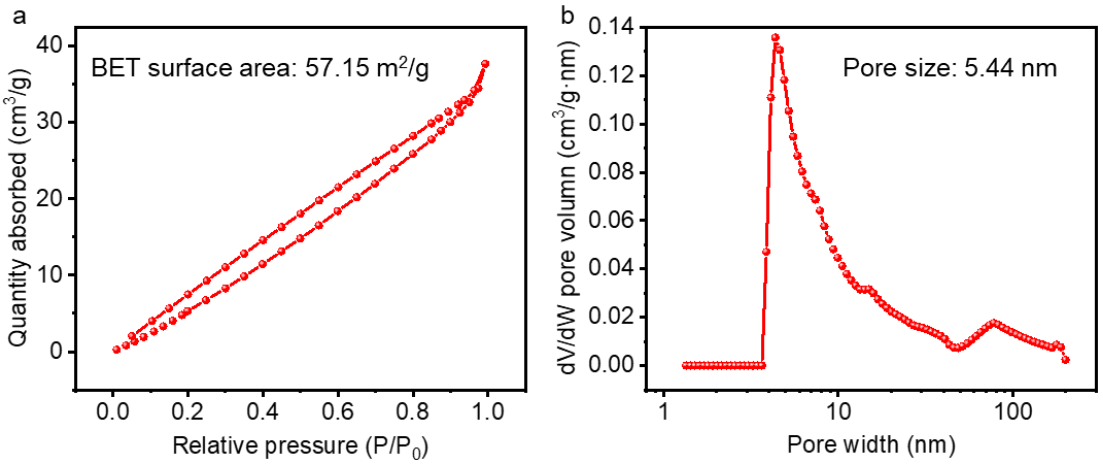

Fig. S24. (a) N_2 adsorption–desorption isotherms and (b) corresponding pore size distribution curves of iHG-PWV samples.

S6. Structure and morphologic characterization of the AuNP@iHG-PWV.

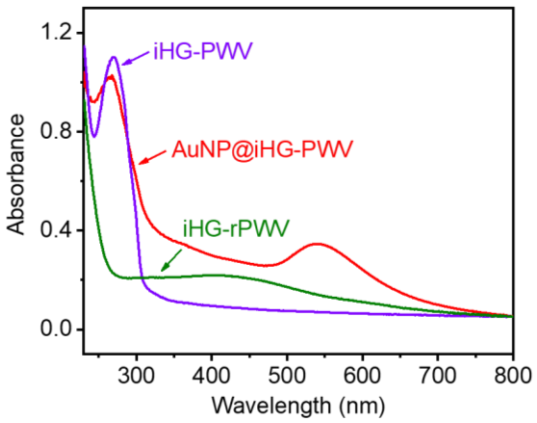

Fig. S25. UV-vis spectra of iHG-PWV, iHG-rPWV and AuNP@iHG-PWV in aqueous solution.

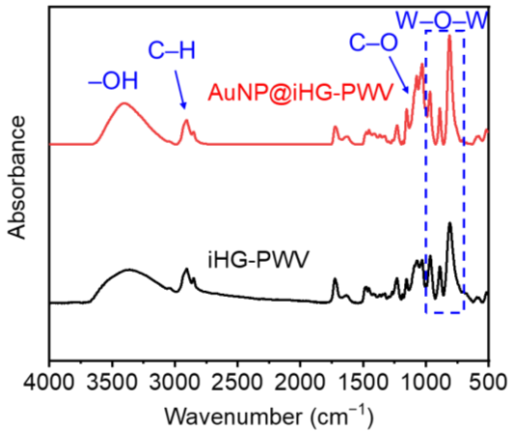

Fig. S26. FT-IR spectra of AuNP@iHG-PWV and iHG-PWV.

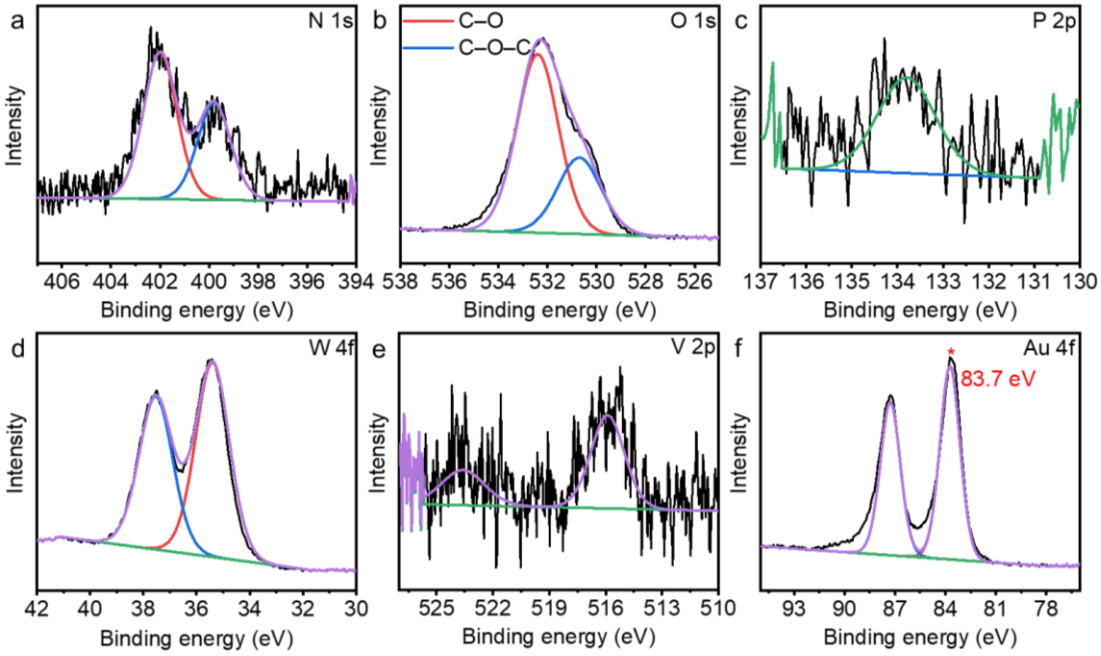

Fig. S27. XPS spectra of (a) N 1s, (b) O 1s, (c) P 2p, (d) W 4f, (e) V 2p, and (f) Au 4f for AuNP@iHG-PWV.

S7. Structure and morphologic characterization of the AuNR@iHG-POM.

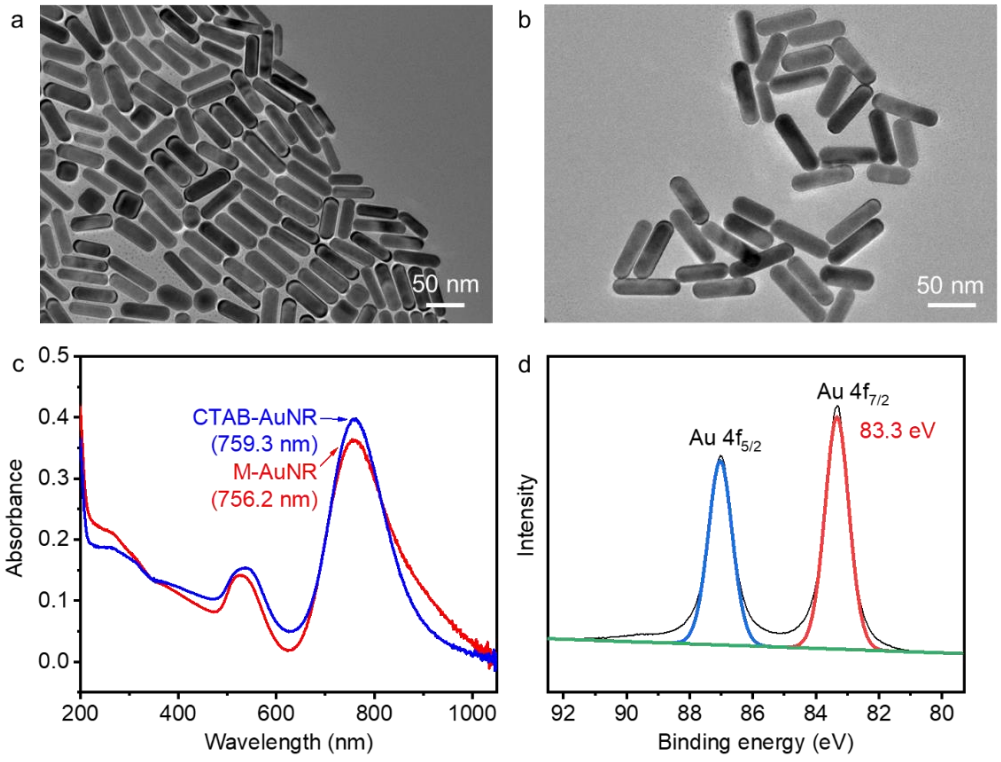

Fig. S28. TEM image of (a) CTAB-AuNRs and (b) M-AuNR. (c) UV-vis spectrum of M-AuNR. (d) XPS spectra of Au 4f for M-AuNR.

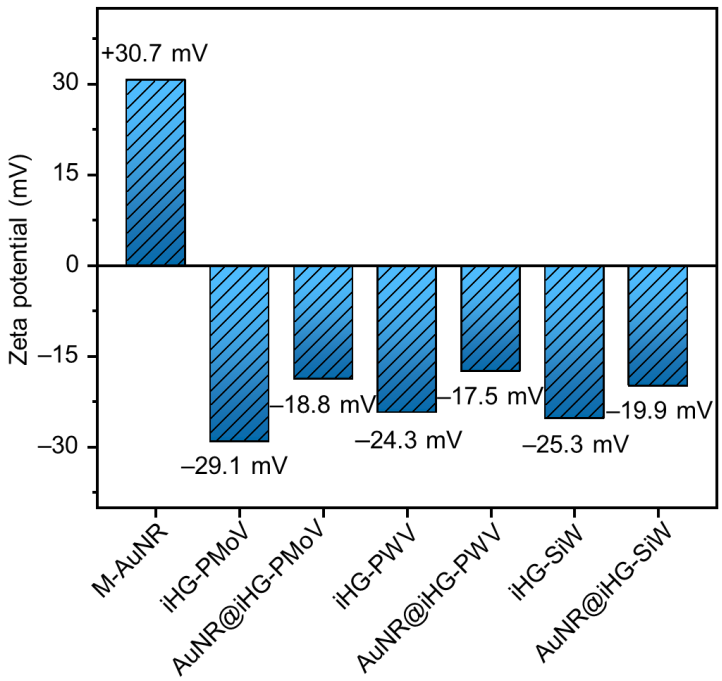

Fig. S29. Zeta potentials of M-AuNR, iHG-PMoV, AuNR@iHG-PMoV, iHG-PWV, AuNR@iHG-PWV, iHG-SiW and AuNR@iHG-SiW in water.

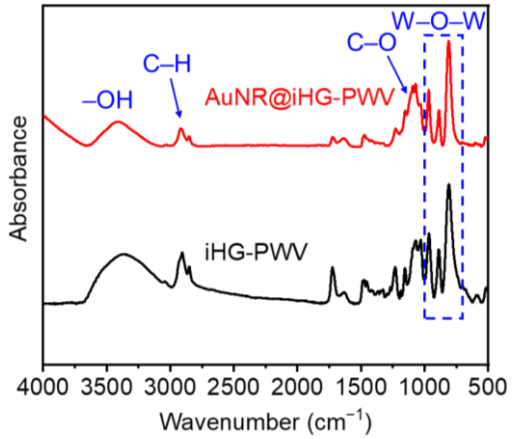

Fig. S30. FT-IR spectra of AuNR@iHG-PWV and iHG-PWV.

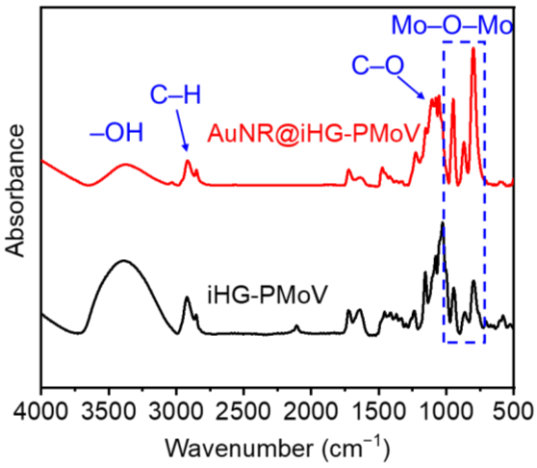

Fig. S31. FT-IR spectra of AuNR@iHG-PMoV and iHG-PMoV.

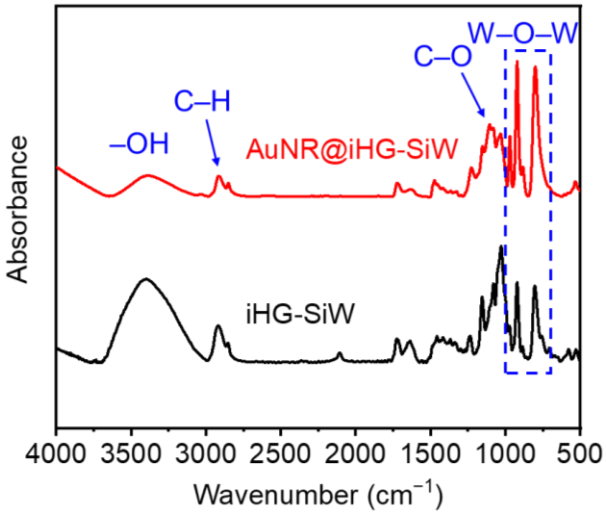

Fig. S32. FT-IR spectra of AuNR@iHG-SiW and iHG-SiW.

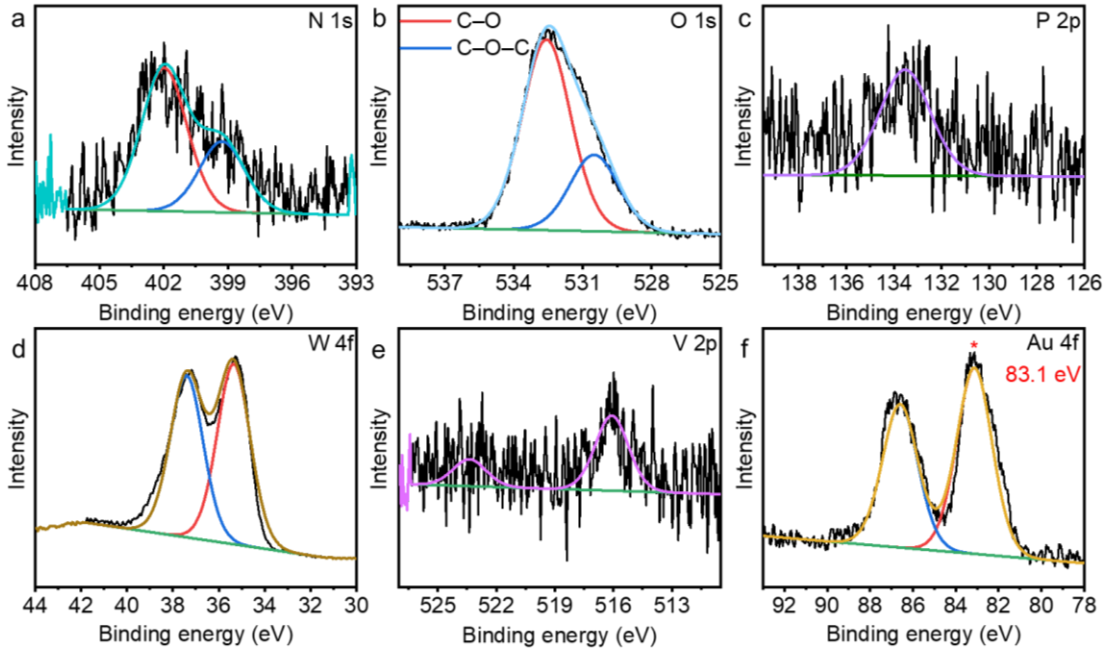

Fig. S33. XPS spectra of (a) N 1s, (b) O 1s, (c) P 2p, (d) W 4f, (e) V 2p and (f) Au 4f for AuNR@iHG-PWV.

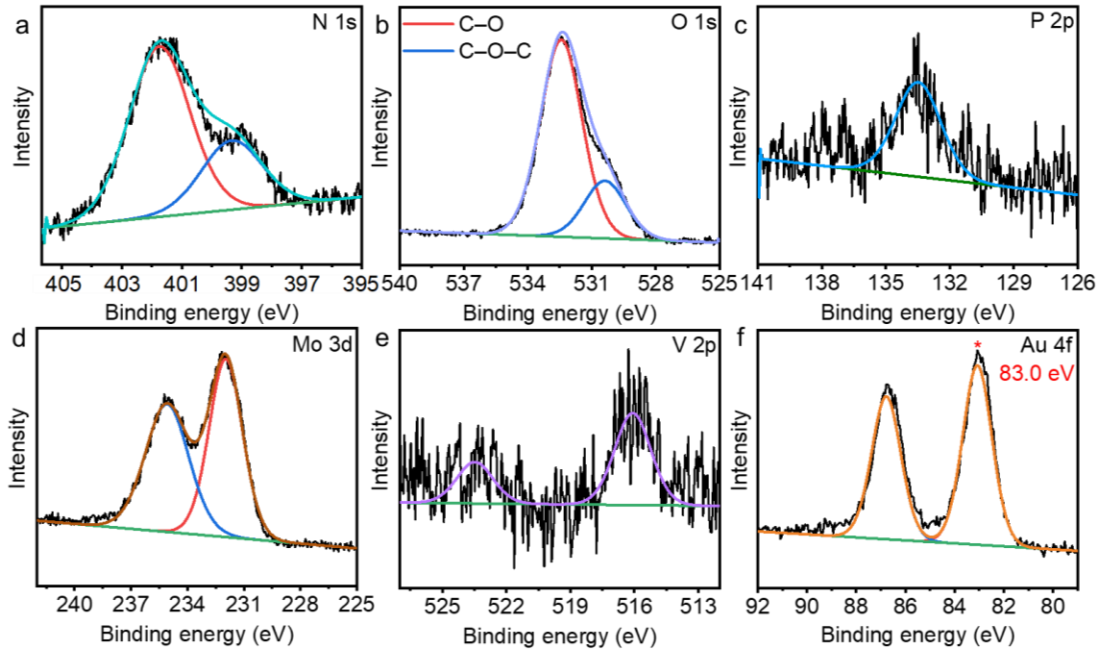

Fig. S34. XPS spectra of (a) N 1s, (b) O 1s, (c) P 2p, (d) Mo 3d, (e) V 2p and (f) Au 4f for AuNR@iHG-PMoV.

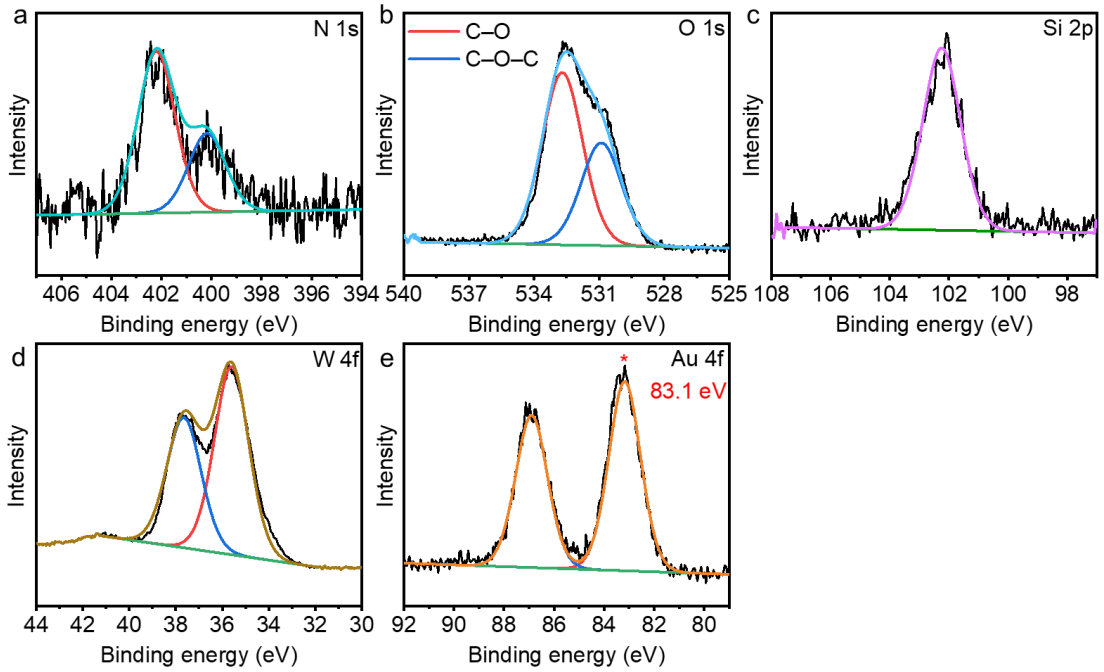

Fig. S35. XPS spectra of (a) N 1s, (b) O 1s, (c) Si 2p, (d) W 4f and (e) Au 4f for AuNR@iHG-SiW.

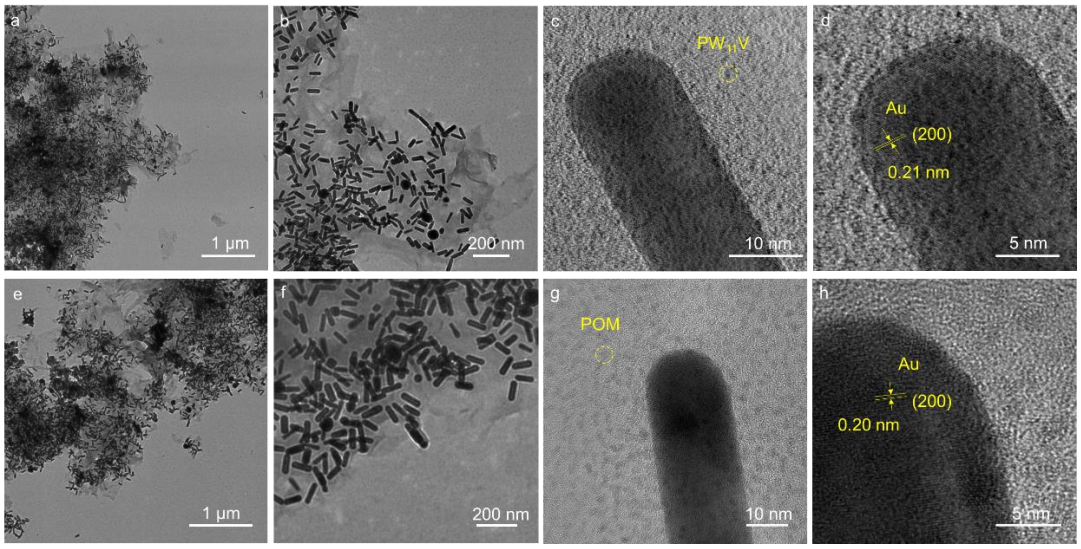

Fig. S36. (a–c) TEM images and (d) HRTEM image of AuNR@iHG-PWV. (e–g) TEM images and (h) HRTEM image of AuNR@iHG-SiW.

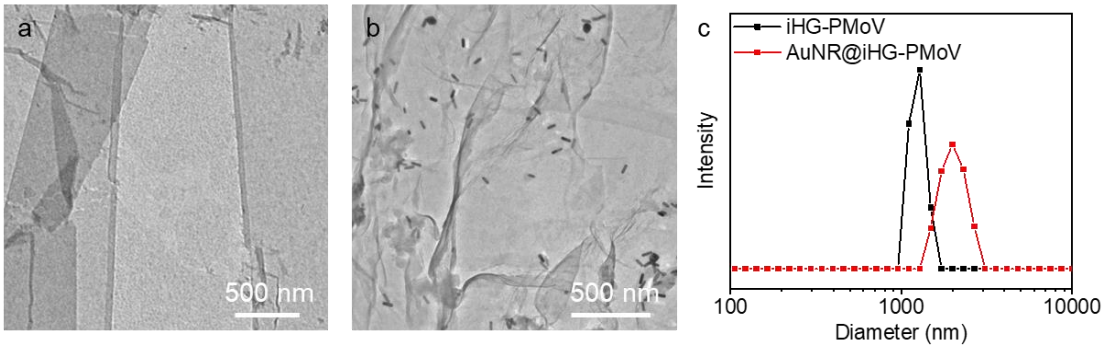

Fig. S37. TEM images of (a) iHG-PMoV and (b)AuNR@iHG-PMoV (assembly preparation: adding dropwise 200 μL of M-AuNR aqueous solution (Au: 135 ppm) to 2.0 mL of iHG-POM solution (2 mL, 0.2 mM)) and DLS diagrams of (c) iHG-PMoV and AuNR@iHG-PMoV in aqueous solution.

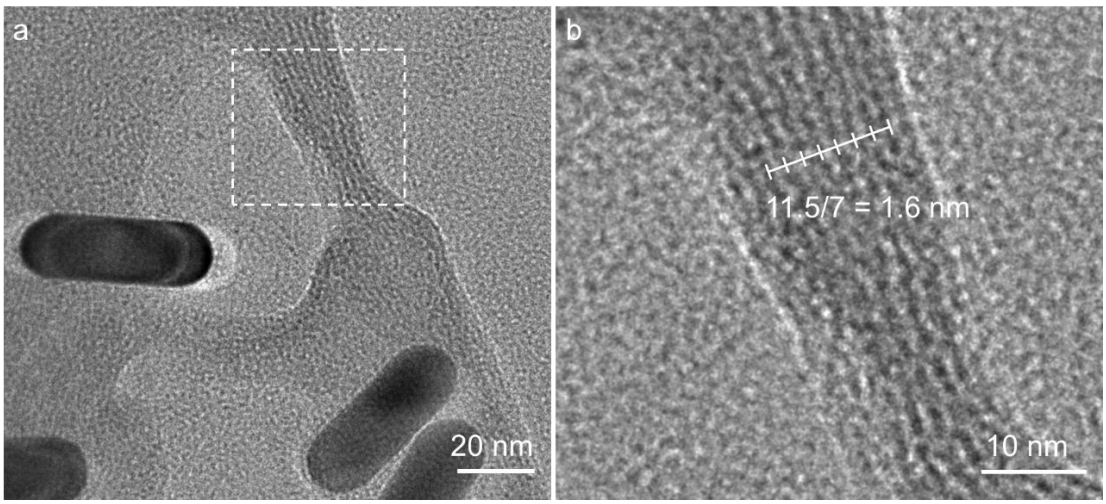

Fig. S38. TEM images of AuNR@iHG-PWV at (a) low and (b) high magnification.

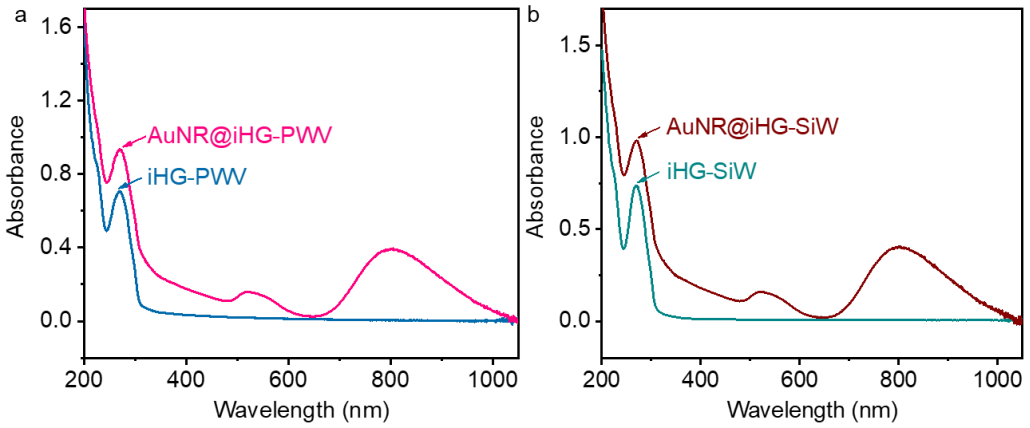

Fig. S39. (a) UV-vis spectra of AuNR@iHG-PWV and iHG-PWV in aqueous solution. (b) UV-vis spectra of AuNR@iHG-SiW and iHG-SiW in aqueous solution.

S8. Photothermal conversion property of the AuNR@iHG-POM.

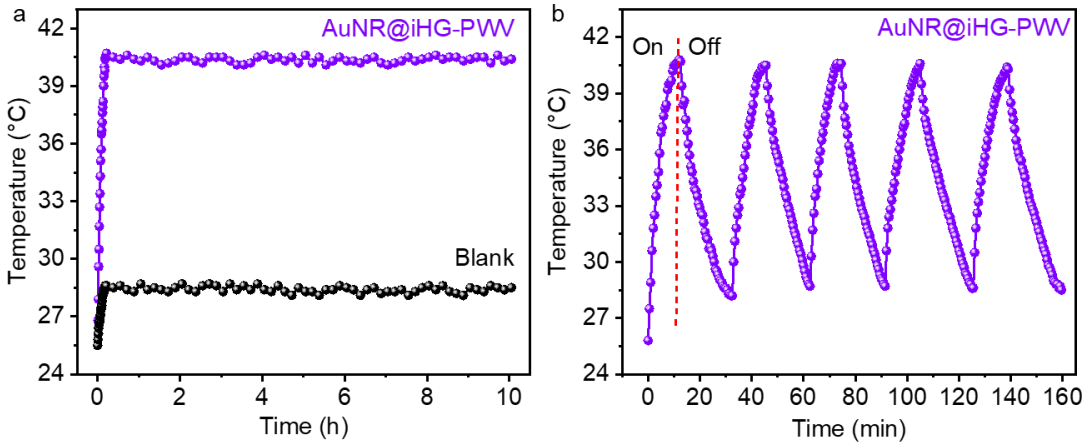

Fig.S40. (a) The temperature variation curve under the continuous irradiation of the NIR laser lamp (808 nm, 1.0 W cm^{-2}). (b) The plot of temperature variation curve of AuNR@iHG-PWV in aqueous solution upon alternate turning on and off the laser in five cycles.

Calculation of the photothermal conversion efficiency of AuNR@iHG-POM.

Taking AuNR@iHG-PWV as an example, the photothermal conversion efficiency is calculated as follows.

• Calculation of the dimensionless driving force temperature (θ).

$$\theta = \frac{T - T_0}{T_{Max} - T_0}$$

Where T is the solution temperature at time t, T_{max} is the highest temperature the solution can reach, T_0 is the starting solution temperature.

• Calculation of the system heat-transfer time constant (τ_s) (Figure S40).

$$\tau_S = -\frac{t}{ln\theta} = 648.52\ s$$

• Calculation of the value of *hS*.

$$hS = \frac{\sum_i m_i C_{p,i}}{\tau_s} = 0.00971$$

Where *h* is the heat transfer coefficient, *S* is the surface area of the container, *m* is the mass of the water, *Cp* is the heat capacity of the water.

• Calculation of the heat released from light absorbed by a container containing pure water (Q_0).

$$Q_0 = \frac{cm\Delta T}{t} = 0.0226\ J \cdot s^{-1}$$

Where ΔT is the temperature drop of the pure water solution after turning off the laser, *t* is heat dissipation time of pure water.

• Calculation of the photothermal conversion efficiency ($\eta_{AuNR@iHG-PWV}$)

$$\eta_{AuNR@iHG-PWV} = \frac{hS(T_{Max} - T_0) - Q_0}{I(1 - 10^{-A_{808}})} = 33.77\%$$

Where *I* is the laser lamp power ($I = 1\ W$), A_{808} is the UV absorbance of the solution at 808nm ($A_{808} = 0.195$).

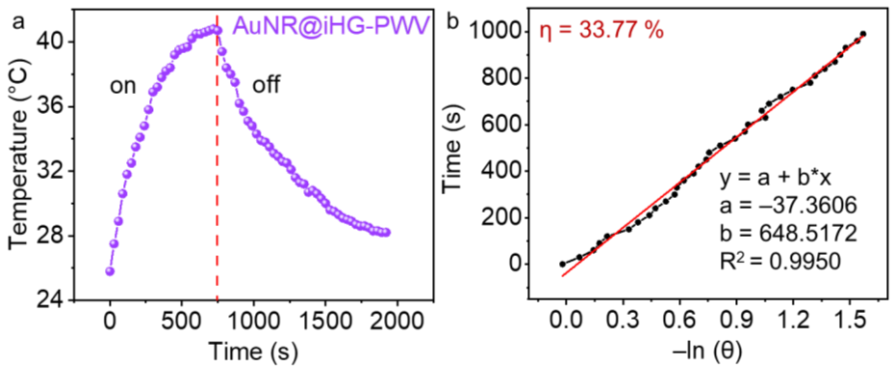

Fig. S41. (a) Temperature variation curve of AuNR@iHG-PWV in aqueous solution irradiated by laser (808 nm, 1.0 W cm^{-2}) on and off versus time and (b) the plot of time versus the –ln (θ) obtained from cooling period.

The photothermal conversion efficiency ($\eta_{AuNR@iHG-PMoV}$) is calculated following the process above.

$$\eta_{AuNR@iHG-PMoV} = \frac{hS(T_{Max} - T_0) - Q_0}{I(1 - 10^{-A_{808}})} = 33.76\%$$

Where I is the laser lamp power ($I = 1\ W$), A_{808} is the UV absorbance of the solution at 808nm ($A_{808} = 0.186$).

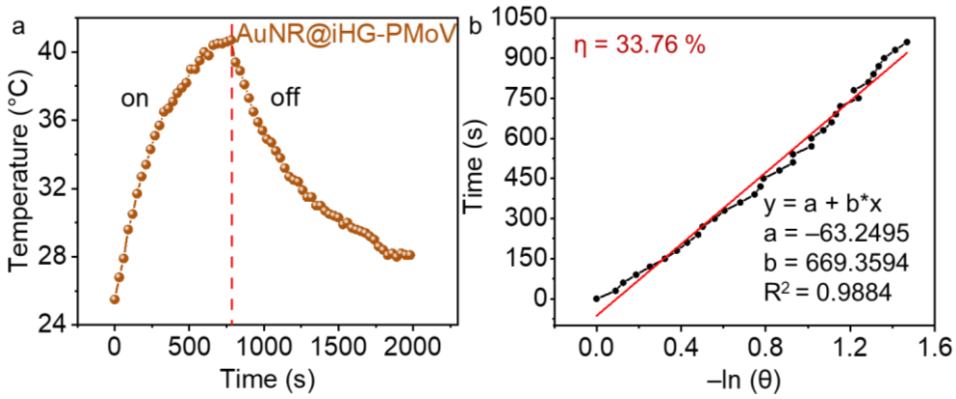

Fig. S42. (a) Temperature variation curve of AuNR@iHG-PMoV in aqueous solution irradiated by laser (808 nm, 1.0 W cm^{-2}) on and off versus time and (b) the plot of time versus the –ln (θ) obtained from cooling period.

The photothermal conversion efficiency ($\eta_{AuNR@iHG-SiW}$) is calculated following the process above.

$$\eta_{AuNR@iHG-SiW} = \frac{hS(T_{Max} - T_0) - Q_0}{I(1 - 10^{-A_{808}})} = 28.8\%$$

Where I is the laser lamp power ($I = 1\ W$), A_{808} is the UV absorbance of the solution at 808nm ($A_{808} = 0.199$).

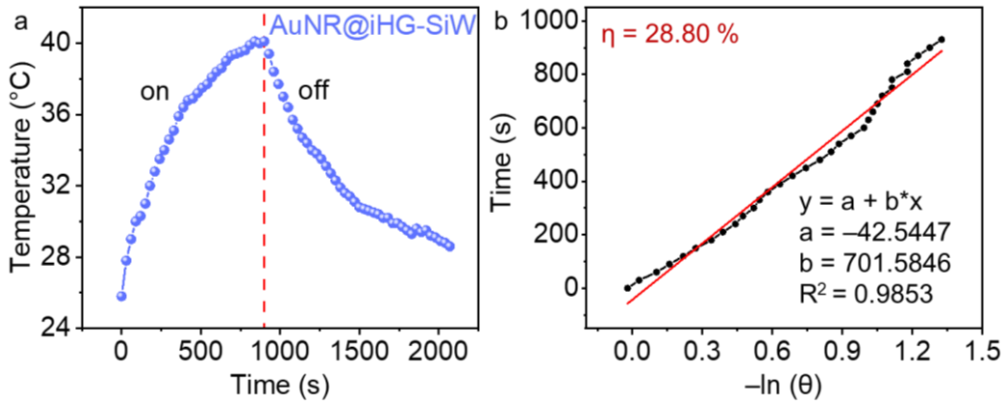

Fig. S43. (a) Temperature variation curve of AuNR@iHG-SiW in aqueous solution irradiated by laser (808 nm, 1.0 W cm^{-2}) on and off versus time and (b) the plot of time versus the –ln (θ) obtained from cooling period.

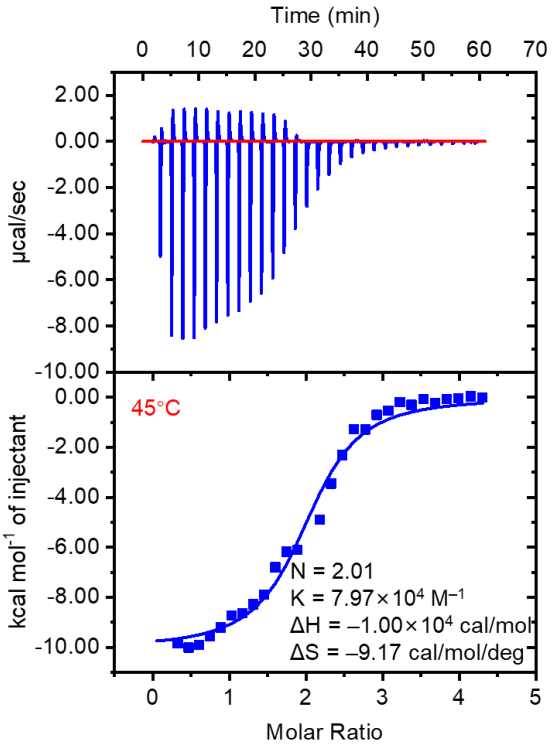

Fig.S44. ITC curves and fittings of C-AD (8 mM) titrating B-CD (0.2 mM) in water at 45°C.

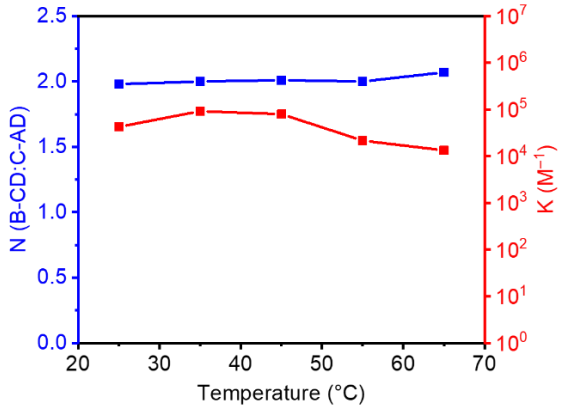

Fig. S45. The binding ratio (blue line) and binding constant (red line) of B-CD and C-AD in aqueous solution versus the temperature.

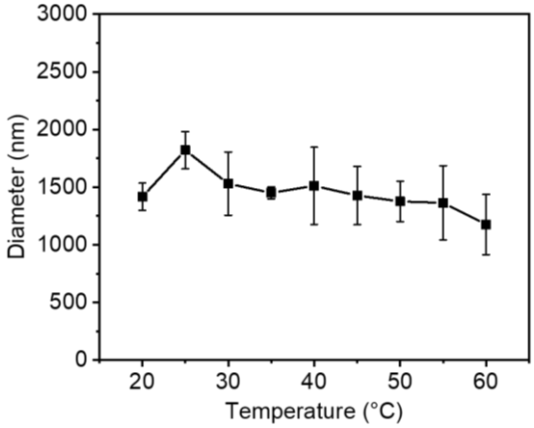

Fig. S46. Plot of size dependence taken from DLS of AuNR@iHG-PWV versus the temperature.

S9. Photocatalysis of N_2 fixation

NH_3 quantification via the indophenol blue method

Under acidic environment, NH_3 reacts with salicylic acid, sodium nitroferricyanide and sodium hypochlorite to produce blue-green indophenol. The reaction equation of this reaction is shown in Scheme S1.

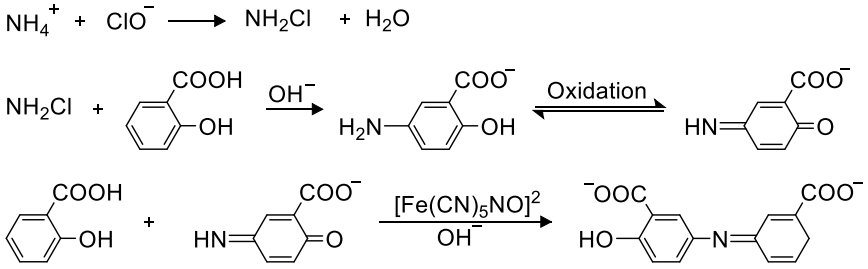

Scheme S4. Ammonia quantification via the indophenol blue method.

Determination of the standard curve. The NH_4Cl standard solution with the NH_4^+ concentration of 1 μg/mL was prepared. 0 mL, 0.25 mL, 0.5 mL, 1 mL, 2 mL, 3 mL, 4 mL and 5 mL of the standard solution was placed in a 10 mL plastic tube respectively, and then diluted to 5 mL. 0.25 mL of salicylic acid solution (5%, 2 M NaOH solution), 0.05 mL of sodium nitroferricyanide solution (1%) and 0.05 mL of sodium hypochlorite solution (0.05M, 2 M NaOH solution) were added sequentially to each solution. After 1 h at room temperature, the solutions were added to a 10 mm quartz cell, and the UV absorbance of each solution at a wavelength of 697.5 nm was determined. The standard curve consistently showed linear relationships between the average absorbance value and NH_3 content (μg) through three independent experiments (Figure S47).

Determination of ammonia content in sample solutions. 5 mL sample solution was mixed with 0.25 mL salicylic acid solution (5%, 2 M NaOH solution), 0.05 mL sodium nitroferricyanide solution (1%) and 0.05 mL sodium hypochlorite solution (0.05M, 2 M NaOH solution). After 1 h at room temperature, the absorbance value of the solution at a wavelength of 697.5 nm was measured. The concentration of NH_3 in solution was calculated according the standard curve.

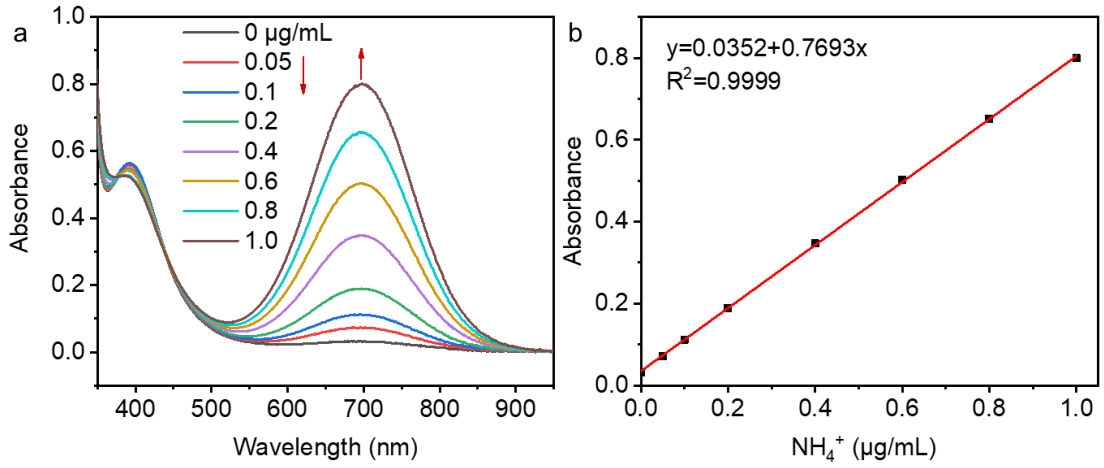

Fig. S47. (a) Titration UV-Vis spectra and (b) plot of absorption versus ammonium concentration for NH_3 quantification using indophenol blue method.

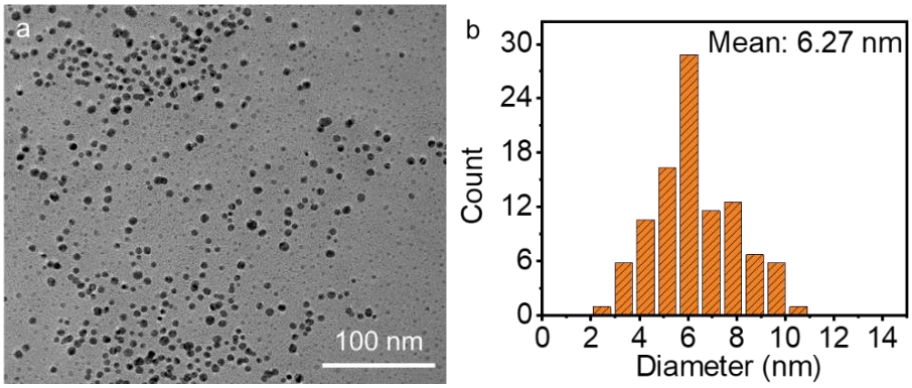

Fig. S48. (a) TEM images of C@AuNPs, and (b) the corresponding statistic histograms of the particle size of C@AuNPs.

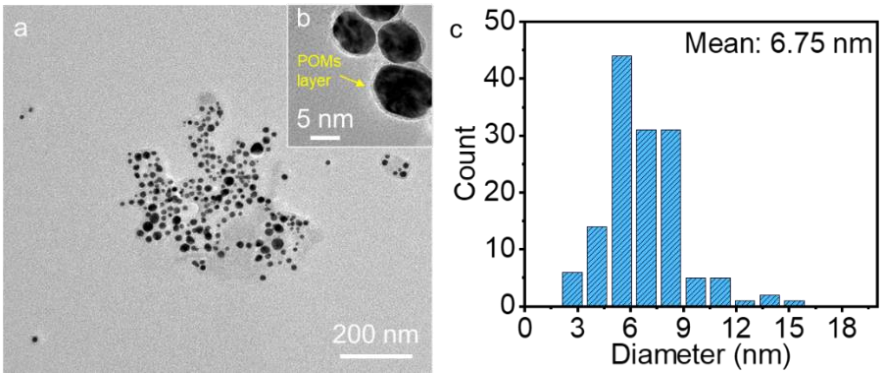

Fig. S49. TEM images of PWV@AuNPs at (a) low and (b) high magnification. (c) The corresponding statistic histograms of the particle size of PWV@AuNPs.

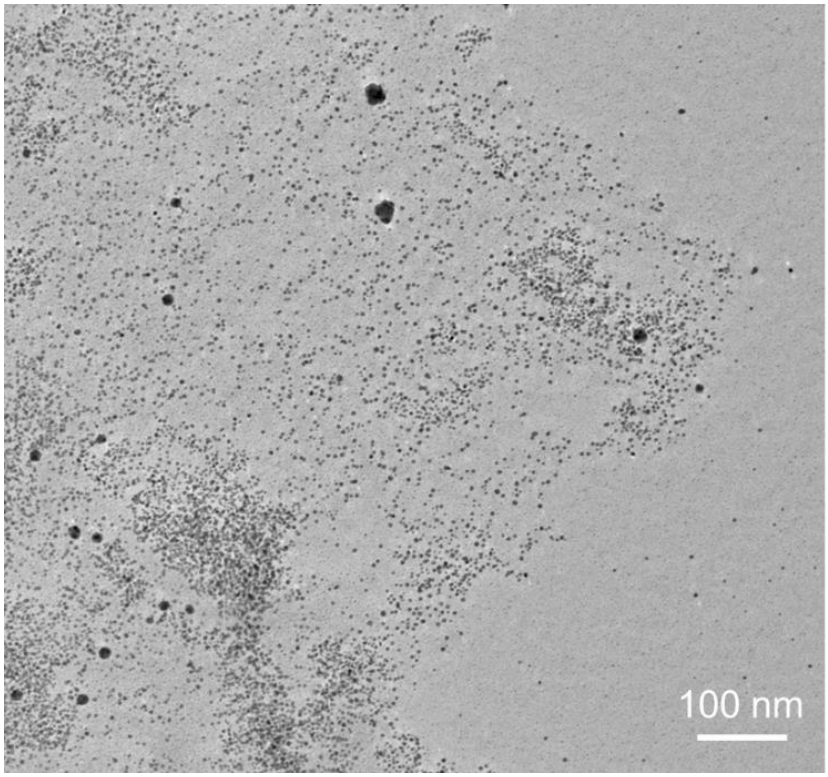

Fig.S50. TEM image of recycled AuNP@iHG-PWV.

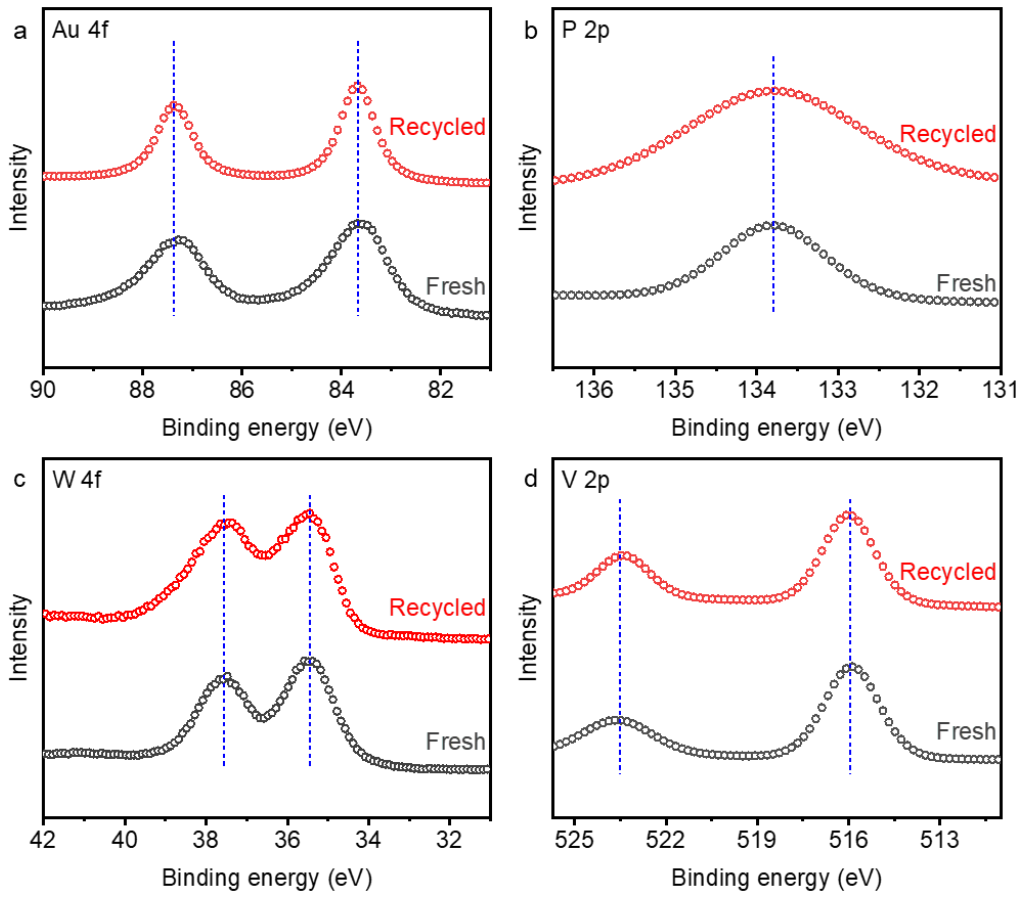

Fig. S51. XPS spectra of (a) Au4f, (b) P2p, (c) W4f, and (d) V2p for recycled and fresh AuNP@iHG-PWV.

Table S4 The results for photocatalytic N_2 fixation in previous literature and our work.

Entry	Catalysts	Reaction conditions	NH_3 production Rate (h^{-1})	TOF (mmol $M^{-1}\cdot h^{-1}$)	Ref.
1	r-GO@$PMo_{10}V_2$	300 W Xe lamp, water	130.3 μmol L^{-1}	207	[7]
2	$P_2W_{17}Co$@V-g-C_3N_4	300 W Xe lamp, water/ethanol	214.6 μmol L^{-1}	346	[8]
3	ZIF-67@PMo_4V_8	300 W Xe lamp, water/ethanol	149.0 μmol L^{-1}	94	[9]
4	100-MIL-101(Cr)-SiW_{12}	300 W Xe lamp, water	75.6 μmol $L^{-1}\cdot g_{cat}^{-1}$	1.95	[10]
5	Au/TiO_2 nanosheet	300 W Xe lamp, water/methanol	78.6 μmol g_{cat}^{-1}	-	[11]
6	CeO_2/AuNR	NIR (808 nm), water/methanol	114.3 μmol g_{cat}^{-1}	-	[12]
7	Au/P25	300 W Xe lamp, water/methanol	1.02 mmol g_{cat}^{-1}	-	[13]
8	Au/g-C_3N_4 hollow sphere	300 W Xe lamp, water/methanol	783.4 μmol g_{cat}^{-1}	-	[14]
9	Au/g-C_3N_4 nanosheet	300 W Xe lamp, water	184 μmol g_{cat}^{-1}	-	[15]
10	Au/Fe TiO_2 nanosphere	300 W Xe lamp, water	49.8 μmol g_{cat}^{-1}	-	[16]
11	Vo-$BaTiO_3$ perovskite	300 W Xe lamp, water	113.5 μmol L^{-1}	-	[17]
12	Ru/RuO_2 C-TiO_x nanosheet	300 W Xe lamp, water/methanol	109.3 μmol g_{cat}^{-1}	-	[18]
13	OVs-Bi_2WO_6 microspheres	300 W Xe lamp, water	53.2 μmol g_{cat}^{-1}		[19]
14	**AuNP@iHG-PWV**	**70 W white LED lamp, water**	**53.7 μmol L^{-1} (84.9 μmol g_{POM}^{-1})**	**235.0**	
15	**AuNR@iHG-PMoV**	**70 W White LED+NIR, water**	**212.4 μmol L^{-1} (616.2 μmol g_{POM}^{-1})**	**1062.1**	
16	**AuNR@iHG-PMoV**		**173.8 μmol L^{-1} (504.2 μmol g_{POM}^{-1})**	**869.1**	**This work**
17	**AuNR@iHG-PWV**	**NIR (808 nm), water**	**70.4 μmol L^{-1} (140.1 μmol g_{POM}^{-1})**	**352.2**	
18	**AuNR@iHG-SiW**		**44.3 μmol L^{-1} (136.0 μmol g_{POM}^{-1})**	**221.5**	

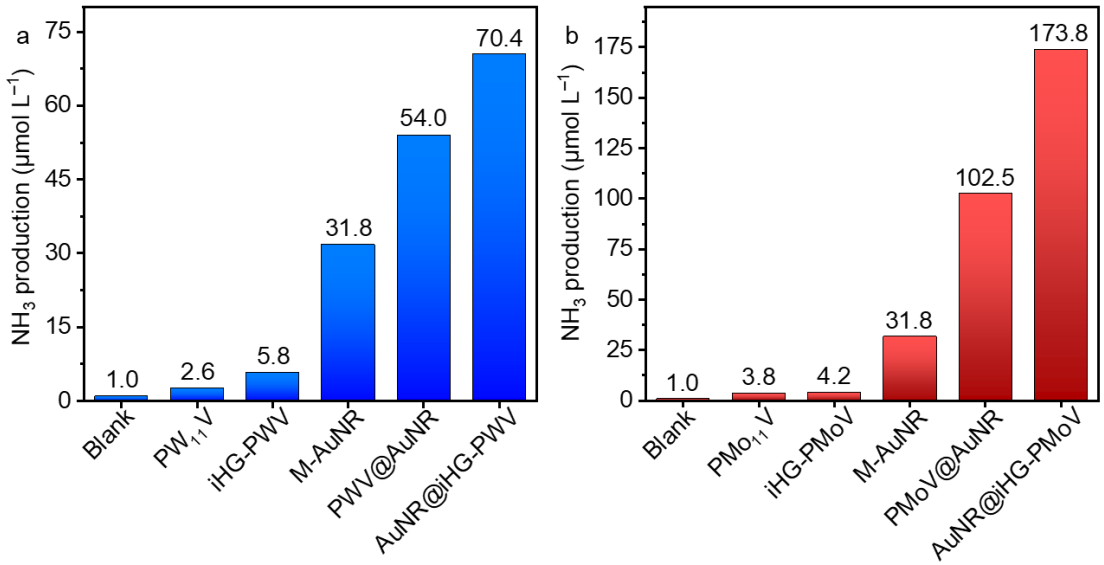

Fig. S52. NH_3 production of N_2 reduction catalyzed by (a) $PW_{11}V$-based catalysts, and (b) $PMo_{11}V$-based catalysts under the irradiation of NIR laser (808 nm, 1.0 W cm^{-2}) for 60 min.

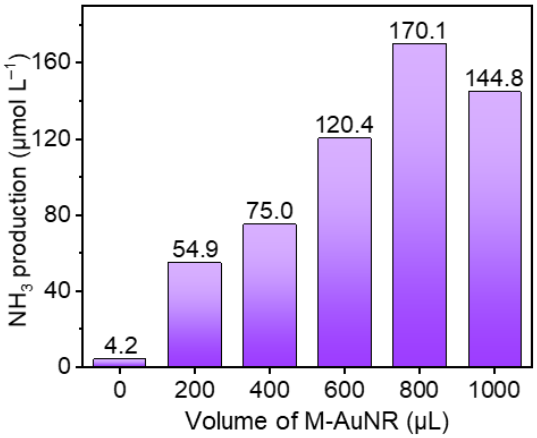

Fig. S53. NH_3 production of N_2 reduction under the irradiation of NIR laser versus the amount of M-AuNRs (Au: 135 ppm) added in iHG-PMoV (2 mL, 0.2mM).

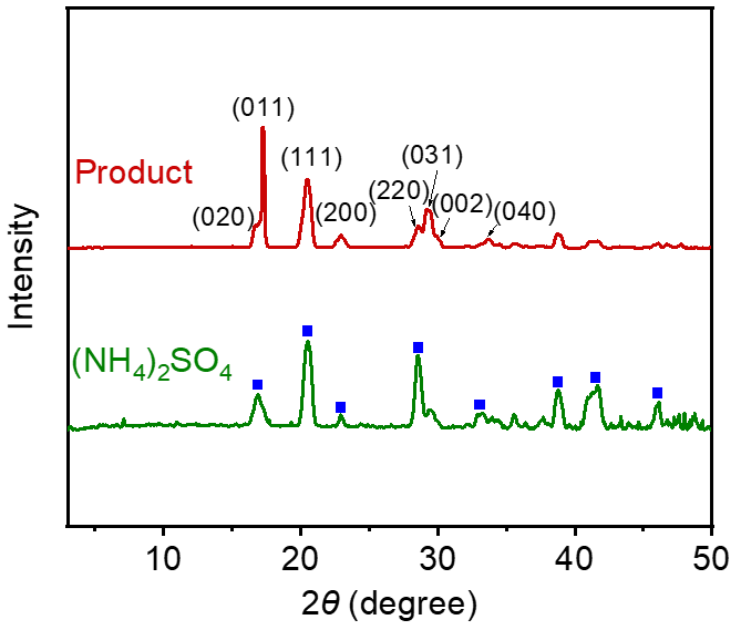

Fig. S54. XRD patterns of the ammonium sulfate and N_2 reduction product catalyzed by AuNR@iHG-PMoV under NIR photothermal condition for 8 days.

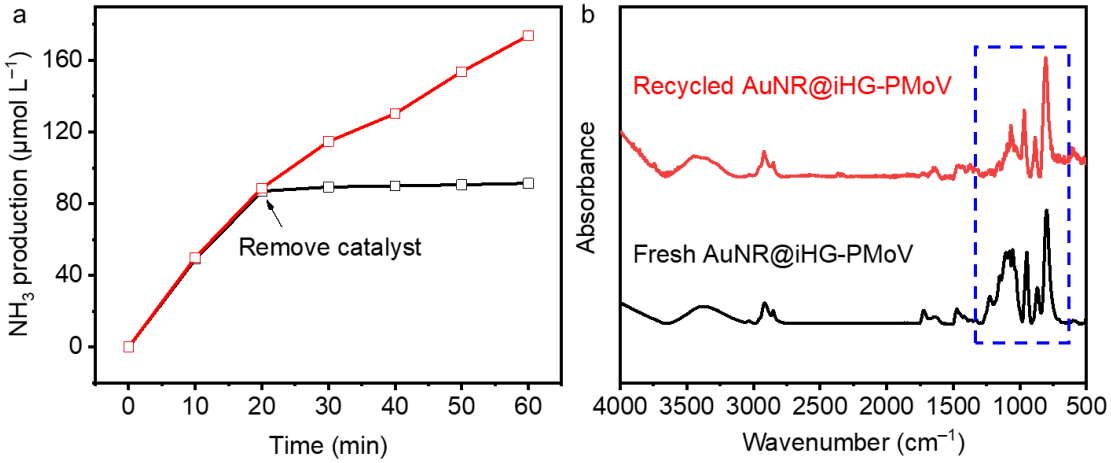

Fig. S55. (a) Leaching test on the NH_3 production in N_2 fixation without and with AuNR@iHG-PMoV as catalyst. (b) FT-IR spectra of the fresh and recycled AuNR@iHG-PMoV.

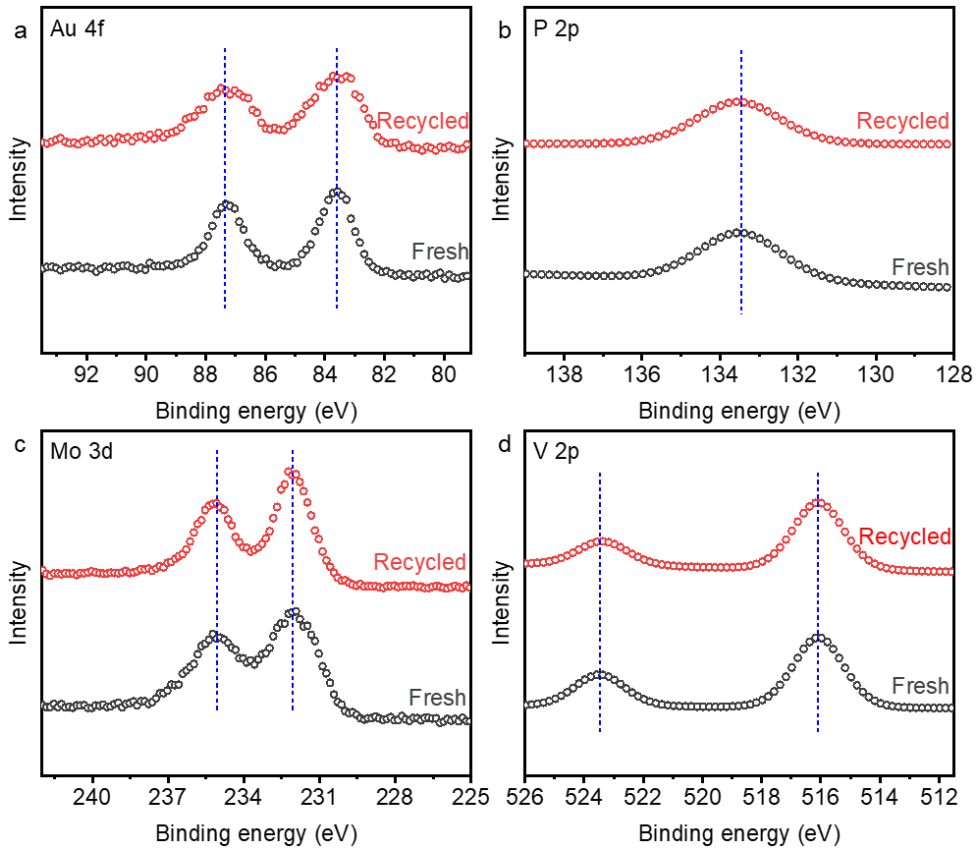

Fig. S56. XPS spectra of (a) Au 4f, (b) P 2p, (c) Mo 3d, and (d) V 2p for recycled and fresh AuNR@iHG-PMoV.

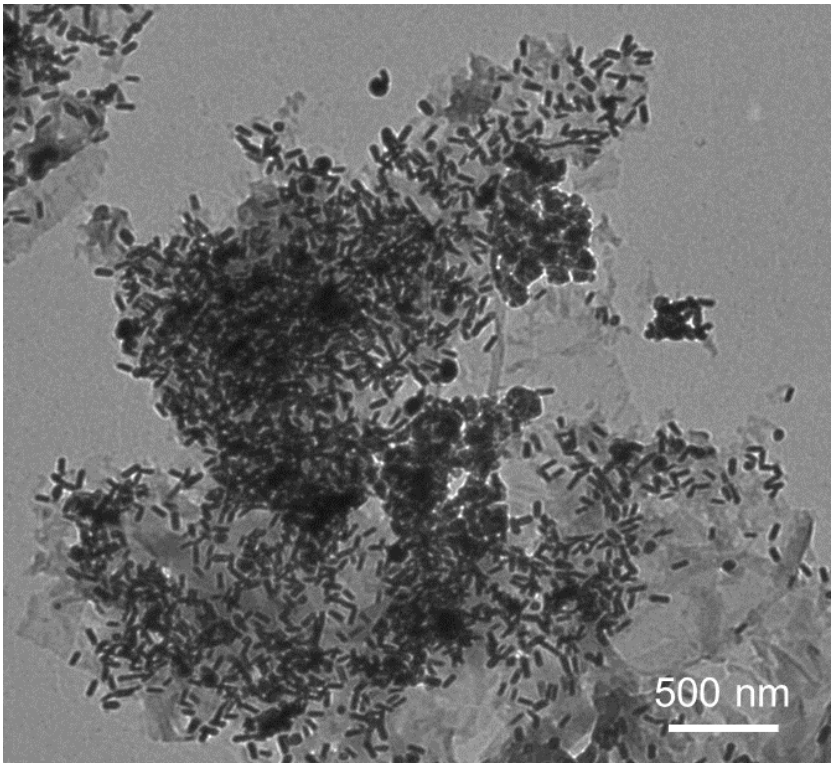

Fig. S57. TEM image for recycled AuNR@iHG-PMoV.

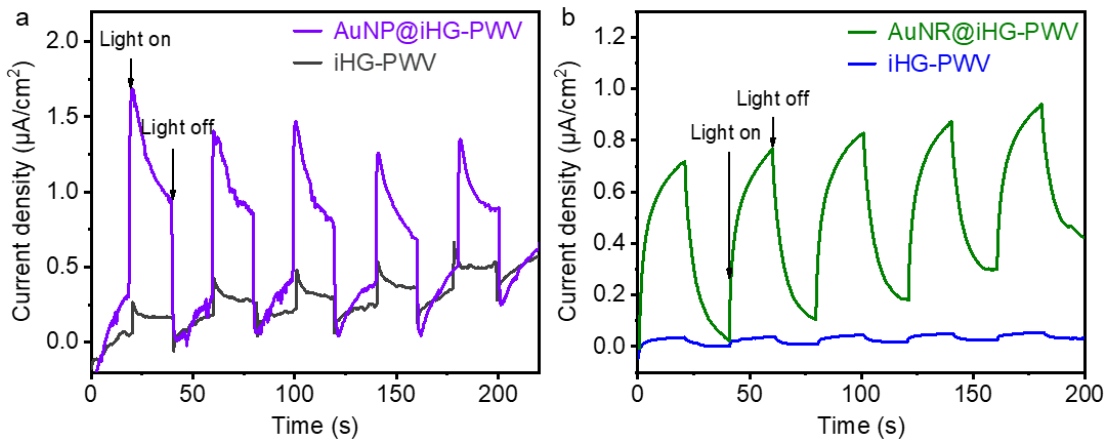

Fig. S58. (a) Photocurrent curves of iHG-PWV and AuNP@iHG-PWV at various time under white LED lamp irradiation. (b) Photocurrent curves of iHG-PWV and AuNR@iHG-PWV at various time under NIR light irradiation.

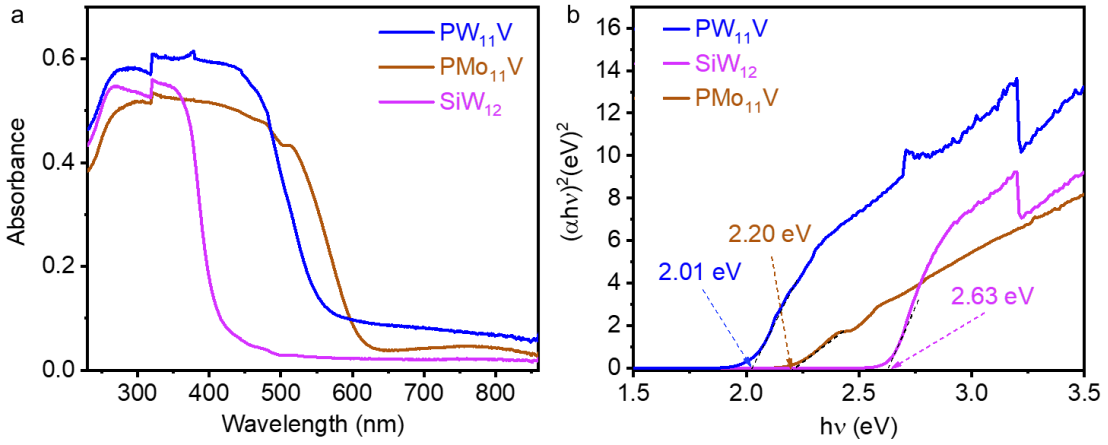

Fig. S59. (a) UV-vis DRS and (b) optical band gap calculation using the Tauc plot method of $PW_{11}V$, $PMo_{11}V$ and SiW_{12}.

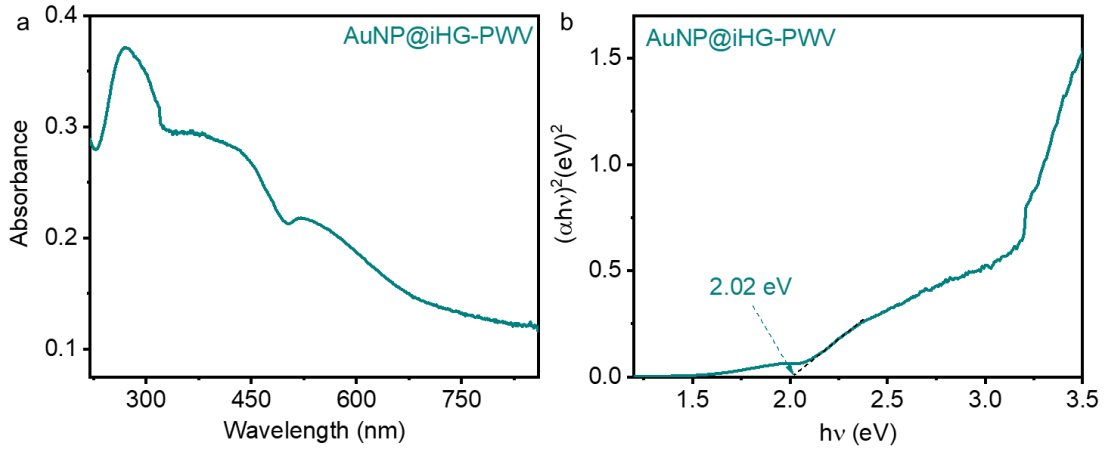

Fig. S60. (a) UV-vis DRS and (b) optical band gap calculation using the Tauc plot method of AuNP@iHG-PWV.

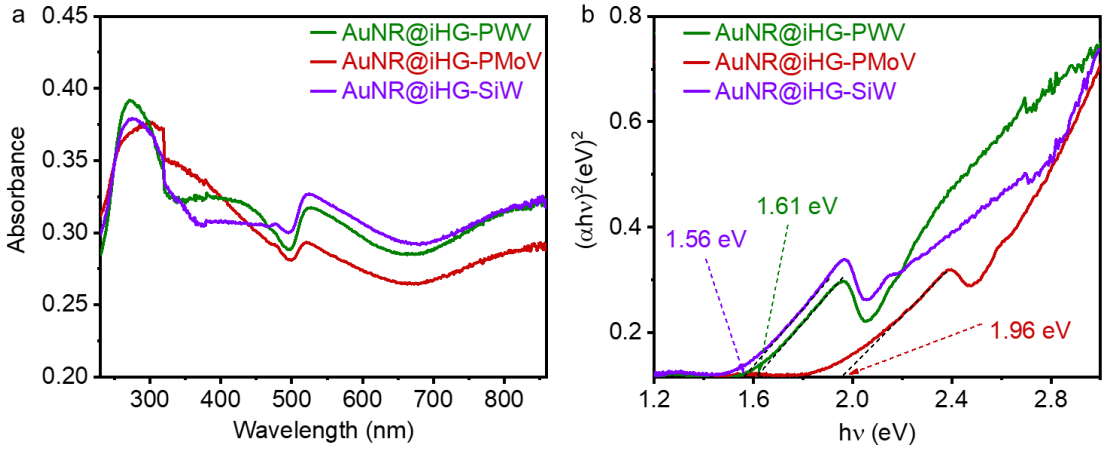

Fig. S61. (a) UV-vis DRS and (b) optical band gap calculation using the Tauc plot method of AuNR@iHG-PWV, AuNR@iHG-PMoV and AuNR@iHG-SiW.

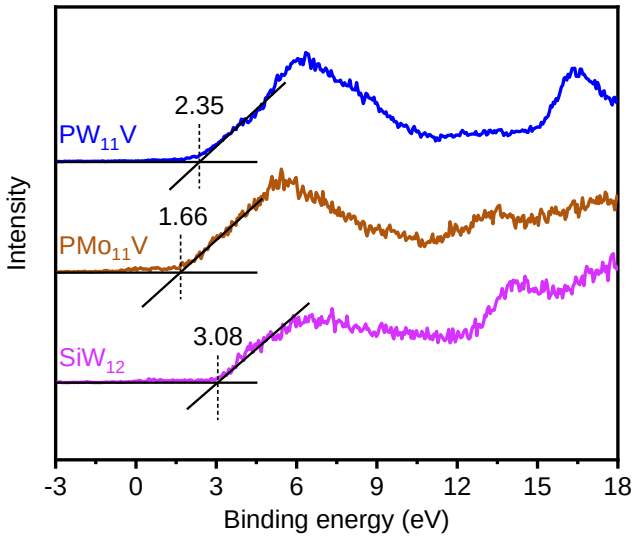

Fig. S62. XPS valence band spectra of $PW_{11}V$, $PMo_{11}V$ and SiW_{12}.

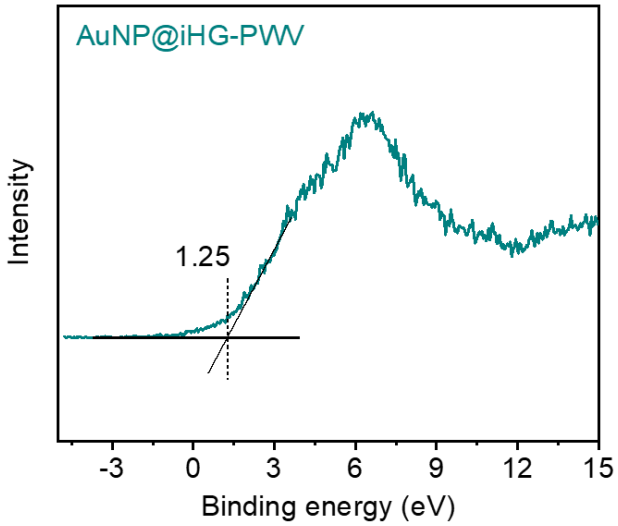

Fig. S63. XPS valence band spectrum of AuNP@iHG-PWV.

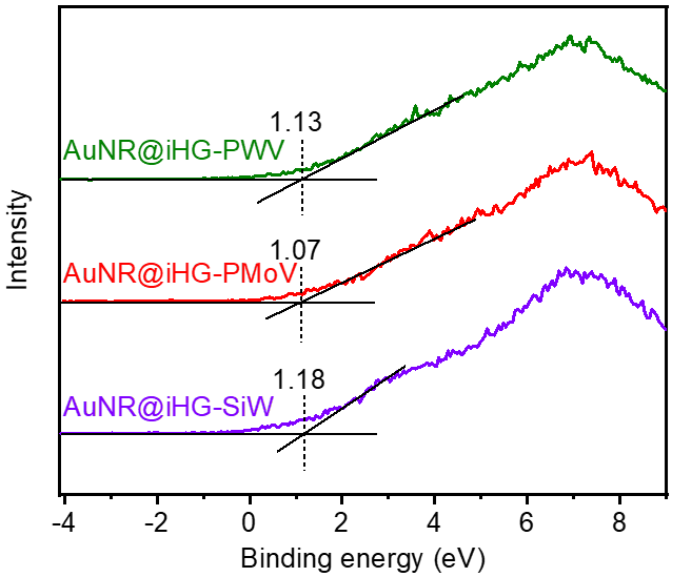

Fig. S64. XPS valence band spectra of AuNR@iHG-PWV, AuNR@iHG-PMoV and AuNR@iHG-SiW.

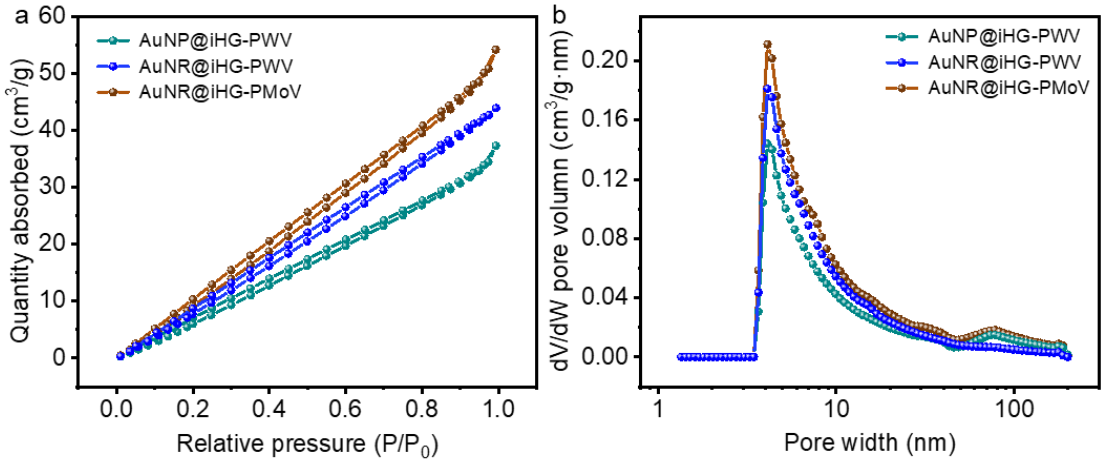

Fig. S65. (a) N_2 adsorption–desorption isotherms and (b) corresponding pore size distribution curves of AuNP@iHG-PWV, AuNR@iHG-PWV and AuNR@iHG-PMoV samples.

Table S5. The results for BET surface area and average size of AuNC@iHG-POM.

Sample	Surface area (m^2/g)	Pore size (nm)
AuNP@iHG-PWV	97.45	5.05
AuNR@iHG-PWV	96.59	4.72
AuNR@iHG-PMoV	84.94	5.07

S10. Reference

[1] P. J. Domaille, *J. Am. Chem. Soc.*, 2002, **106**, 7677–7687.

[2] G. A. Tsigdinos, C. J. Hallada, *Inorg. Chem.*, 2002, **7**, 437–441.

[3] Russell C. Petter, Jeffrey S. Salek, Christopher T. Sikorski, G. Kumaravel, and Fu-Tyan Lin, *J. Am. Chem. Soc.*, 1990, **112**, 3860–3868.
[4] Y. Wang, H. Li, C. Wu, Y. Yang, L. Shi, L. Wu, *Angew. Chem. Int. Ed.*, 2013, **52**, 4577–4581.
[5] G. X. Wang, B. Li, L. X. Wu, *J. Mater. Chem. A*, 2022, **10**, 21884.
[6] P. Thordarson, *Chem. Soc. Rev.*, 2011, **40**, 1305–1323.
[7] X. H. Li, W. L. Chen, H. Q. Tan, F. R. Li, J. P. Li, Y. G. Li, E. B. Wang, *ACS Appl. Mater. Interfaces*, 2019, **11**, 37927–37938.
[8] X.-H. Li, W.-L. Chen, P. He, T. Wang, D. Liu, Y.-W. Li, Y.-G. Li, E.-B. Wang, *Inorg. Chem. Front.*, 2019, **6**, 3315–3326.
[9] X. H. Li, P. He, T. Wang, X. W. Zhang, W. L. Chen, Y. G. Li, *ChemSusChem*, 2020, **13**, 2769–2778.
[10] S. Su, X. Li, X. Zhang, J. Zhu, G. Liu, M. Tan, Y. Wang, M. Luo, *J. Colloid Interface Sci.*, 2022, **621**, 406-415.
[11] J. Yang, Y. Guo, R. Jiang, F. Qin, H. Zhang, W. Lu, J. Wang, J. C. Yu, *J. Am. Chem. Soc.*, 2018, **140**, 8497–8508.
[12] H. Jia, A. Du, H. Zhang, J. Yang, R. Jiang, J. Wang, C. Y. Zhang, *J. Am. Chem. Soc.*, 2019, **141**, 5083–5086.
[13] T. A. Bu, Y. C. Hao, W. Y. Gao, X. Su, L. W. Chen, N. Zhang, A. X. Yin, *Nanoscale*, 2019, **11**, 10072–10079.
[14] Y. Guo, J. Yang, D. Wu, H. Bai, Z. Yang, J. Wang, B. Yang, *J. Mater. Chem. A*, 2020, **8**, 16218–16231.
[15] S. Wu, Z. Chen, K. Liu, W. Yue, L. Wang, J. Zhang, *ChemSusChem,* 2020, **13**, 3455–3461.
[16] J. Yang, H. Bai, Y. Guo, H. Zhang, R. Jiang, B. Yang, J. Wang, J. C. Yu, *Angew. Chem. Int. Ed.*, 2021, **60**, 927–936.
[17] Z. Zhao, D. Wang, R. Gao, G. Wen, M. Feng, G. Song, J. Zhu, D. Luo, H. Tan, X. Ge, W. Zhang, Y. Zhang, L. Zheng, H. Li, Z. Chen, *Angew. Chem. Int. Ed.*, 2021, **60**, 11910–11918.
[18] Q. Han, C. Wu, H. Jiao, R. Xu, Y. Wang, J. Xie, Q. Guo, J. Tang, *Adv. Mater.*, 2021, **33**, e2008180.
[19] T. Wang, C. Feng, J. Liu, D. Wang, H. Hu, J. Hu, Z. Chen, G. Xue, *Chem. Eng. J.*, 2021, **414**, 128827.